

Copyright Warning & Restrictions

The copyright law of the United States (Title 17, United States Code) governs the making of photocopies or other reproductions of copyrighted material.

Under certain conditions specified in the law, libraries and archives are authorized to furnish a photocopy or other reproduction. One of these specified conditions is that the photocopy or reproduction is not to be “used for any purpose other than private study, scholarship, or research.” If a user makes a request for, or later uses, a photocopy or reproduction for purposes in excess of “fair use” that user may be liable for copyright infringement,

This institution reserves the right to refuse to accept a copying order if, in its judgment, fulfillment of the order would involve violation of copyright law.

Please Note: The author retains the copyright while the New Jersey Institute of Technology reserves the right to distribute this thesis or dissertation

Printing note: If you do not wish to print this page, then select “Pages from: first page # to: last page #” on the print dialog screen

The Van Houten library has removed some of the personal information and all signatures from the approval page and biographical sketches of theses and dissertations in order to protect the identity of NJIT graduates and faculty.

ABSTRACT

DIRECT SIMULATION OF ELECTORRHEOLOGICAL SUSPENSIONS SUBJECTED TO PRESSURE DRIVEN FLOW AND SPATIALLY NON- UNIFORM ELECTRIC FIELD

by

Arun Thankamony John Kadaksham

A numerical method based on the distributed Lagrange Multiplier method is developed for direct simulation of electrorheological (ER) suspensions subjected to pressure driven flows and spatially non-uniform electric fields. The flow inside particle boundaries is constrained to be rigid body motion by the distributed Lagrange multiplier method and the point-dipole approximation is used to model the electrostatic forces acting on the polarized particles. Simulations show that the particles move to the regions of high electric field when the value of β , the Clausius-Mossotti factor is positive and they move to the regions of low electric field when the value of β is negative. Also, dielectrophoretic force can be used for separating particles with different β values.

Using the simulation method the evolution of the microstructure under the influence of electrostatic forces (particle-particle interaction force and dielectrophoretic force) and hydrodynamic forces is analyzed. The different microstructures formed are explained on the basis of non-dimensional parameters that determine the relative strength of the various forces. Simulations show that even when the particle-particle interaction force, dielectrophoretic force and hydrodynamic force co-exists, the parameters can be judiciously manipulated so that either the yield stress and viscosity of the ER fluid increases or the particles get collected in the regions of low or high electric fields.

**DIRECT SIMULATION OF ELECTORRHEOLOGICAL SUSPENSIONS
SUBJECTED TO PRESSURE DRIVEN FLOW AND SPATIALLY NON-
UNIFORM ELECTRIC FIELD**

**by
Arun Thankamony John Kadaksham**

**A Thesis
Submitted to the Faculty of
New Jersey Institute of Technology
in Partial Fulfillment of the Requirements for the Degree of
Master of Science in Mechanical Engineering**

Department of Mechanical Engineering

May 2003

Blank Page

APPROVAL PAGE

**DIRECT SIMULATION OF ELECTORRHEOLOGICAL SUSPENSIONS
SUBJECTED TO PRESSURE DRIVEN FLOW AND SPATIALLY NON-
UNIFORM ELECTRIC FIELD**

Arun Thankamony John Kadaksham

Dr. Pushendra Singh, Thesis Advisor

Date

Associate Professor of Mechanical Engineering, NJIT

Dr. Nadine N. Aubry, Committee Member

Date

Professor of Mechanical Engineering, NJIT

Dr. Anthony D. Rosato, Committee Member

Date

Professor of Mechanical Engineering, NJIT

BIOGRAPHICAL SKETCH

Author: Arun Thankamony John Kadaksham

Degree: Master of Science

Date: January 2003

Undergraduate and Graduate Education:

- Master of Science in Mechanical Engineering,
New Jersey Institute of Technology, Newark, NJ, USA, 2003
- Bachelor of Technology in Mechanical Engineering,
University of Kerala, India, 1998

Major: Mechanical Engineering

Presentations and Publications:

- J. Kadaksham, P.Singh and N. Aubry,
“Direct simulation of electrorheological fluids subjected to spatially nonuniform electric fields,” ASME 2002.
- J. Kadaksham, P.Singh and N. Aubry,
“Dynamics of electrorheological suspensions subjected to spatially nonuniform electric fields,” 14th US National Congress of Theoretical and Applied Mechanics Proceedings, Virginia Polytechnic Institute and State University, Blacksburg, VA, June 23-28, 2002.
- J. Kadaksham, J. Batton, P.Singh, N. Golubovic-Liakopoulos and N. Aubry,
“Dielectrophoretic manipulation of micro- and nano-scale particles in micro-channels,” Nanotechnology World Forum 2003.
- J. Kadaksham, J. Batton, P. Singh, N. Golubovic-Liakopoulos and N. Aubry,
“Micro-fluidic platform for manipulating micro- and nano-scale particles,” 2003 ASME International Mechanical Engineering Conference and R&D Expo, Washington, D.C., USA, November 15-21, 2003.

J. Kadaksham, P.Singh and N. Aubry,
“Dynamics of particles in electrorheological suspensions subjected to dielectrophoretic forces”, Submitted for Publication in Journal of Fluids Engineering, (2003).

J. Kadaksham, P.Singh and N. Aubry,
“Dynamics of electrorheological suspensions subjected to spatially varying electric fields”, Submitted for publication in Journal of Fluids Engineering (2003).

To my parents.

ACKNOWLEDGMENT

I would like to thank my advisor, Dr. Pushpendra Singh, for all his guidance and support throughout the research of this work. This work would have remained incomplete without his great interest as well as methodology. I would like to pay special thanks to Dr. Pushpendra Singh for putting in his time and efforts and encouraging me to achieve all that I have.

I would also like to extend my sincere gratitude to the members of my committee, Dr. Nadine Aubry and Dr. Anthony Rosato. I am particularly appreciative of their effort in reviewing my work on such short notice.

I gratefully acknowledge the support of the New Jersey Commission on Science and Technology through the New Jersey Center for Micro-Flow Control for the financial support I had during this work.

Last but not the least; I would like to thank my family and friends for all their support.

TABLE OF CONTENTS

Chapter	Page
1 INTRODUCTION.....	1
1.1 Electrorheology.....	1
1.2 Dielectrophoresis.....	6
2 GOVERNING EQUATIONS.....	11
2.1 Electrostatic Forces.....	11
2.2 Governing Equations for the Fluid and the Particles.....	13
2.3 Dimensionless Parameters.....	15
3 FINITE ELEMENT METHOD.....	18
3.1 The Computational Scheme.....	18
3.2 Collision Strategy.....	20
3.3 Time Discretization Using the Marchuk-Yanenko Operator Splitting Scheme.....	21
4 NUMERICAL RESULTS.....	25
4.1 Uniform Electric Field.....	28
4.1.1 Convergence.....	28
4.1.2 Effect of Hydrodynamic and Electrostatic Forces on ER Fluids.....	30
4.1.3 Time Evolution of Particle-Scale Structure with no Imposed Flow.....	33
4.1.4 Behavior of 105 Particles in a Channel Subjected to Pressure Driven Flow.....	38
4.2 NON-UNIFORM ELECTRIC FIELD.....	41
4.2.1 Convergence.....	41
4.2.2 Cases with $dp/dz = 0$	45

TABLE OF CONTENTS
(Continued)

Chapter	Page
4.2.3 Cases with $dp/dz \neq 0$	55
4.2.4 Mixture Containing Particles with Positive and Negative β	61
4.2.5 Influence of Electric Potential Boundary Condition	66
4.2.6 Variation with P_4	70
5 CONCLUSIONS	75
REFERENCES	77

LIST OF FIGURES

Figure	Page
4.1.a An oblique view of the typical domain used for simulations.....	25
4.1.1.a Figure showing the initial arrangement of particles for the convergence study. In pressure driven flows the chains get bend as shown. The figure shown is not to scale	28
4.1.1.b The z-component of the velocity w for the middle particle is shown for different values of mesh sizes.....	29
4.1.1.c The z-coordinate of middle particle is plotted for different values of time steps	30
4.1.2 Electric field strength, a. 3×10^2 , b. 6×10^2 , c. 1×10^3 , d. 3×10^3	32
4.1.3 Particle positions at different times, a. $t = 0$ s, b. $t = 0.035$ s, c. $t = 0.08$ s, d. $t = 0.08$ s.....	35
4.1.3.e Initial staggered position of the particles	37
4.1.3.f Straight chains at time $t = 0.035$ s	37
4.1.3.g Oriented chains as seen from the xy plane at time $t = 0.2$ s	37
4.1.3.h zy view of column formation.....	37
4.1.3.i zx view of column formation.....	37
4.1.3.j Columns moving to sidewalls.....	37
4.1.4.a Straight chains formed at $t = 0.08$ s	39
4.1.4.b Parabolic chains	39
4.1.4.c Straight chains converted to parabolic ones at $t = 0.15$ s due to the imposed flow	39
4.1.4.d Chains merging together to form columns.....	39
4.2.1.a Isovalues of $\log(\mathbf{E})$ and the direction of \mathbf{E} on the domain midsection are shown. Notice that the electric field is maximum on the electrode	

LIST OF FIGURES
(Continued)

Figure	Page
tips. The electric field does not vary with y	41
4.2.1.b Isovalues of $\log(\mathbf{E} \cdot \nabla \mathbf{E})$ and the direction of dielectrophoretic force on the domain midsection are shown	41
4.2.1.c The domain mid section normal to the y -axis is shown. The domain width along the y -direction is 0.4 mm. The cross-section is the same for all values of y . Also shown are the electrode locations and the initial positions of the two particles. The potential is prescribed on the electrode surfaces and the normal derivative of the potential is assumed to be zero on the rest of the boundary. The velocity is assumed to be periodic in the z -direction and zero on the other domain surfaces	42
4.2.1.d The z coordinate of the middle particle is plotted for four different values of time step. Notice that the results for the smallest two time steps are approximately the same which indicates that the results converge with time step refinement	43
4.2.1.e The z -coordinate of the second particle plotted as a function of time for three different mesh sizes. The particle positions for the two finer meshes are virtually identical implying that the results converge with mesh refinement	44
4.2.2.a The initial particle positions on the midsection normal to the y -direction	45
4.2.2.b Isovalues of the $\log(\mathbf{E})$ on the domain midsection	46
4.2.2.c Isovalues of $\log(\mathbf{E} \cdot \nabla \mathbf{E})$ and lines of dielectrophoretic force	46
4.2.2.d The top view of the particle distribution at $t = 0.20$ s for $\beta = +0.297$	50
4.2.2.e The top view of the particle distribution at $t = 0.70$ s for $\beta = +0.297$	50
4.2.2.f The top view of the particle distribution at $t = 11.0$ s for $\beta = +0.297$	50
4.2.2.g An oblique view of the particle distribution at $t = 13.3$ s for $\beta = +0.297$	50
4.2.2.h The top view of the particle distribution at $t = 0.2$ s for $\beta = -0.297$	51

**LIST OF FIGURES
(Continued)**

Figure	Page
4.2.2.i The top view of the particle distribution at $t = 0.85$ s for $\beta = -0.297$	51
4.2.2.j The top view of the particle distribution at $t \sim 12$ s for $\beta = -0.297$	52
4.2.2.k The top view of the particle distribution at $t = 16.4$ s.....	52
4.2.2.l A typical experimental setup showing the electrodes and the channel.....	54
4.2.2.m ER fluid when initially introduced in the channel.....	54
4.2.2.n Particles collected at the edges of the electrodes in 1 minute.....	54
4.2.2.o Particles collected after 3 minutes	54
4.2.3.a The top view of the particle distribution at $t = 0.45$ s for $\beta = 0.297$ and pressure gradient $dp/dz = 1$ dyne/cm ³ . Notice that the particles collect near the electrodes	57
4.2.3.b $t = 0.8$ s for $\beta = 0.297$ and the pressure gradient $dp/dz = 1$ dyne/cm ³ . Notice the curved, concave down, chains near the center.....	57
4.2.3.c $t = 1.5$ s for $\beta = 0.297$ and the pressure gradient $dp/dz = 1$ dyne/cm ³ . Notice the curved, convex up, chains.....	57
4.2.3.d The top view of the particle distribution at $t = 0.5$ s for the pressure gradient $dp/dz = 5$ dynes/cm ³ and $\beta = 0.297$	60
4.2.3.e $t = 1.0$ s. The white particles, even though close to the electrodes, are being pushed downstream by the flow	60
4.2.3.f $t = 1.40$ s. The white particles are moving away from the electrodes, while getting closer to each other.....	60
4.2.3.g $t = 2.0$ s. The white particles are now captured by the lower electrodes	60
4.2.4.a An oblique view of the initial position of particles with $\beta < 0$ and $\beta > 0$	63
4.2.4.b The top view of particle distribution at $t = 0.3$ s.....	63

LIST OF FIGURES
(Continued)

Figure	Page
4.2.4.c $t = 0.5$ s	63
4.2.4.d $t = 0.8$ s.....	63
4.2.4.e $t = 2.5$ s.....	64
4.2.4.f $t \sim 14$ s	64
4.2.4.g Isovalues of $\log(\mathbf{E})$ and the direction of \mathbf{E} on the domain midsection are shown	65
4.2.4.h Isovalues of $\log(\mathbf{E} \cdot \nabla \mathbf{E})$ and the lines of dielectrophoretic force.....	65
4.2.4.i The final position of the particles collected at $t = 3$ s.....	65
4.2.5.a The top view of the particle distribution at $t = 3$ s for $\beta < 0$	68
4.2.5.b The position of the particles collected	68
4.2.5.c The particles being collected at the minimum of the electric field.....	69
4.2.6.a The top view of the particle distribution at $t = 4.0$ s for the case where $P_4 = 0.03$	73
4.2.6.b The top view of the particle distribution at time $t = 1.25$ s for the case where $P_4 = 2.7$	73
4.2.6.c An oblique view of particles collected near the electrodes edges at $t = 5.29$ s	73
4.2.6.d An oblique view of particle chains at $t = 3.08$ s.....	73

CHAPTER 1

INTRODUCTION

1.1 Electrorheology

A study of electrorheological (ER) suspensions is important because it is possible to change their rheological transport properties as well as the structure at particle scales by externally applying an electric field. In fact, the rheological properties of these fluids can be reversibly altered by several orders of magnitude by the application of an electric field, with magnitudes of the order of KV/mm. They can be used in a wide range of applications that require fluids with changeable transport properties, and so at least in principle, they can function as smart fluids.

A typical ER suspension consists of an insulating liquid medium with an insulating/semi-conducting particulate material or liquid material suspended in it. The change in rheological properties occurs because of the rapid rearrangement of the suspended particles in the direction of the electric field, which is reversible. Historical origins of the study of electrorheology can be traced back to the 19th century when the application of an electric field was found to alter the viscosity of some pure insulating liquids [12]. This effect, which was then termed the electroviscous effect, was further investigated by Andrade and coworkers during the 1950's [3].

Winslow [60] was the first to experimentally study the electrorheological effects in suspensions of non-conducting and semi-conducting particles in a media of low conductivity. He was the first to introduce the concept of “fibrillous” chain structure formation in the electrorheological fluid on the application of an electric field, which is responsible for the increase in viscosity of the suspension. After Winslow several models

were proposed to explain the formation of fibrillated chain structure in ER fluids. Early models include the electric double layer model [33, 57], which was further extended by Stangroom [51, 52] to include the effect of water in the structure formation.

Marshall, Goodwin and Zukoski performed experimental studies of ER fluids [41] for wide ranges of shear rates, field strengths and volume fractions and proposed the dependence of the relative suspension viscosity of the ER fluid on the Mason number, which is the ratio of viscous forces to the electrostatic polarization forces acting on the particles of the suspension. Zukoski and co-workers performed elaborate experimental studies [17, 63] on ER fluids which laid the foundation to much of the later research in the field of electrorheology.

The invention of anhydrous ER fluids resulted in a need to explain the phenomena of electrorheology in a way other than the water bridge mechanism which banks on the water presence in the ER suspension to explain the formation of chains. Much of the work was focused on finding the electrostatic polarization force acting on the particles of a chain. A model for estimating the polarization of particles based on the dielectric constant mismatch between the suspended particles and the suspending medium was proposed in [37, 44]. The polarization model, along with the point-dipole approximation, was widely used to explain many experimental phenomena observed in ER fluids. Theoretical studies based on this polarization model have been used to study idealized ER fluids containing spherical, monodispersed and non-conducting particles and a non-conducting suspending medium [2, 35-38]. As just noted, the point-dipole approximation is used to model the particle-particle interaction forces but it ignores many body interactions. In some of these studies the Stokes drag law is used to approximate the

hydrodynamic forces acting on the particles and the Brownian forces acting on the particles are ignored. The latter is appropriate for suspensions containing large sized particles.

Davis used the point-dipole approximation to analyze ER behavior and reported the first finite element simulation study in the area of ER research [12-14]. Adriani et al. modeled ER fluid as a concentrated suspension of hard spheres with aligned field-induced dipole moments [1] to determine the rheological response to a high frequency, small amplitude, oscillatory flow.

Tao et al. proposed a bct structure for the ground state of the columns formed in the ER suspension under the application of an electric field [23, 54, 55] and later performed simulations with Brownian force included along with electrostatic and hydrodynamic interactions and verified the evolving bct structure [56].

The ER research that witnessed a slowdown after Winslow, was later revived during the early eighties and nineties, primarily due to the great interest shown by the industries, especially the automotive industry on the devices that were proposed based on the ER effect such as brakes, clutches, valves, etc. Most of the devices proposed failed to materialize commercially due to a poor understanding of the ER mechanisms and the failure in controlling the behavior of the ER suspensions in the required manner.

In recent years, there is a revived interest in electrorheology due to the advent of nanotechnology and nanomaterials and our ability to better understand and simulate the behavior of ER fluids. Many models have been proposed that capture the behavior of ER fluids in real time and many numerical simulation studies have been done based on these models. For example, the point-dipole approximation has been used extensively in

computer simulations [34-36, 38, 44] because of its simplicity and ease of use. However, it errs considerably because the approximations made in obtaining it are not valid for concentrated suspensions and thus, it falls short of the observed experimental behavior in many cases. Klingenberg et al. made ad-hoc corrections to improve its accuracy. See, et al. made use of the polarization model to perform simulations of ER fluids and explained the dependence of the shear stress of the ER fluid on the frequency of applied electric field [46] and also tried to explain the role of water contained in the ER suspension in determining its viscosity [47, 48].

Recently, a dipole-induced-dipole model was developed for computer simulations of poly-dispersed ER fluids [50]. Here a “multiple image method” is used to compute the inter-particle forces between particles of different properties and sizes.

The failure of polarization model in explaining certain observed rheological phenomena resulted in the development of conduction model by Atten and Foulc [4, 16, 53, 61, 62] in which the ER effect was assumed to be dependent on the particle and liquid conductivities. Later, Khusid and Acrivos [32] developed the model to include dynamic events before the suspension microstructure is fully developed. They study the effect of conductivity of both the particles and the fluid in the initial stages of formation of the structure in ER fluids. They show theoretically that at low dc electric fields conductivity effects determine the interparticle interactions and results in slow aggregation, whereas at high dc electric fields rapid aggregation takes place since the conductivity effects do not contribute much to the interparticle interactions.

The conduction model has its own drawbacks and T. Hao and coworkers came up with a dielectric loss model [24-28], which depends on the particle dielectric loss to

explain the chain formation. According to the dielectric loss model, there are two dynamic processes that determine the evolution of structure in ER fluids. The first step is the particle polarization determined by the particle dielectric constant and the second step is the orientation of the particles along the direction of the electric field determined by the particle dielectric loss. As per this model, the observed ER effect and the formation of chains depend on the ability of the particles to reorient in the direction of the electric field, which in turn depends on the particle dielectric loss tangent.

Several numerical studies have been performed using the above models for electrostatic forces combined with hydrodynamic models to numerically simulate the steady state behavior, as well as the transient response of ER fluids, in simple shear flows [7-9, 35-38]. In these simulations, the trajectories of particles were obtained by integrating Newton's second law, as is done in the molecular dynamic studies of liquids. The Reynolds number in these studies was assumed to be zero. The exact hydrodynamic forces acting on the particles, as well as the particle-particle and fluid-particle interactions, in this limit, were computed using the Stokesian dynamics approach [8-10]. Specifically, simulations were performed for a planer mono-layer containing 25 spherical particles subjected to simple shear flows. In Refs. [8-10] the drag force acting on a particle was approximated by the Stokes drag law but the number of particles was much larger. This approximation ignores not only the inertial effects, as the Stokes law is valid only for an isolated particle in the limit of zero Reynolds number, but also the influence of the particles on the fluid as well as the particle-particle interactions. Furthermore, the accuracy of this approximation is expected to decrease with increasing particle concentration and therefore it is likely to break down in the regions where the particle

concentration is high, e.g., in the regions containing particle chains and columns, and also where particles agglomerate in the case of non-uniform electric field. Tamura et al. [47, 48] used a similar approach to study the rheological properties of hydrous ER suspensions in which they also accounted for the forces due to the water bridges.

The results of these numerical studies have also been used for developing phenomenological models that relate the rheological properties and the particle-scale structure of ER suspensions. Lukkarnen and Kaski [39] studied the mechanical properties of ER fluids under various dynamical loading conditions, and Gong and Lim [19] explored the cases where the loading is either perpendicular or parallel to the electric field, which corresponds to the shear or tensile straining. These studies have been helpful in increasing our understanding of the ER response of fluids.

1.2 Dielectrophoresis

Dielectrophoresis is defined to be the translational motion of neutral particles in a non-uniform electric field caused by polarization effects [31, 45]. This motion is a result of the dielectrophoretic (DEP) force, which acts on a polarizable particle in a non-uniform electric field. Note that when a dielectric particle is subjected to a uniform external electric field it gets polarized and thus also interacts with the other particles via the electrostatic particle-particle interaction forces. Thus, in a non-uniform electric field the particles are subjected to both the particle-particle interactions and the dielectrophoretic force.

The particle scale structures for the spatially uniform and varying electric fields are quite different as in the latter case dielectrophoretic force also acts on the particles. In

the former case, the distribution of particles remains quasi uniform and the particles form chains that are aligned parallel to the electric field direction. In the latter case, the particle distribution becomes non-uniform and the particles agglomerate either near or away from the electrodes, depending on the sign of $\beta = \frac{\epsilon_p - \epsilon_c}{\epsilon_p + 2\epsilon_c}$, where ϵ_c and ϵ_p are the dielectric

constants of the liquid and particles. This property, as will be discussed later, can be used for removing and separating undesirable particles from liquids.

The DEP force experienced by a particle in a non-uniform electric field is given by

$$\mathbf{F}_{\text{DEP}} = 4\pi a^3 \epsilon_0 \epsilon_c \beta \mathbf{E} \cdot \nabla \mathbf{E} \quad (1)$$

where a is the particle radius, $\beta = \frac{\epsilon_p - \epsilon_c}{\epsilon_p + 2\epsilon_c}$ is the Clausius-Mossotti factor, ϵ_c and ϵ_p being

the dielectric constants of the fluid and the particles, $\epsilon_0 = 8.8542 \times 10^{-12}$ F/m is the permittivity of free space and \mathbf{E} is the electric field. From this expression it can be noted that when β is positive the direction of the dielectrophoretic force is along the gradient of the magnitude of electric field and when β is negative the force acts in the opposite direction. Moreover, since the polarizability of particles is frequency dependent, the DEP force is also frequency dependent [20].

It is worth noting that the direction of the dielectrophoretic force determines the regions in which the particles agglomerate. For example, when β is positive the dielectrophoretic force tend to move the particles to the regions where the electric field strength is locally maximum which is normally on the electrode surfaces. On the other

hand, when β is negative the particles move to the regions where the electric field strength is locally minimum. The dielectrophoretic force, therefore, tends to make the particle distribution in an ER liquid less uniform and thus can have a dramatic impact on its structure and macroscopic transport properties.

Since the direction and magnitude of the dielectrophoretic force depends on the dielectric properties, it can be effectively used for the separation of particles with different dielectric properties [22]. Moreover since the permittivity is frequency dependent, by simply selecting a suitable frequency and a suitable fluid, different kinds of particles may be separated.

The above fact has been demonstrated and has been utilized for the separation and characterization of bacterial cells [40] and also for applications such as separation of cancer cells from human blood [5, 6].

The micro-fabrication techniques developed during the past two decades, such as photolithography and etching, have made easy the manufacturing of microelectrodes and microchannels of different shapes which in turn has helped in the manipulation of microparticles, as well as in understanding the phenomenon in a greater depth [20]. Bulk of the research related to applications of dielectrophoretic techniques have been bio-medical oriented. Specifically, Morgan et al. [56] experimentally studied the manipulation and separation of submicron latex spheres and viruses by applying high gradient electric field generated by microelectrodes. The technique has been used also for separating DNA molecules and proteins [58]. In certain cases, dielectrophoretic techniques were employed to study the dielectric properties of pathogens such as viruses [30]. Here the dielectrophoretic properties were obtained as a function of the applied

frequency and the conductivity of the suspending medium. Specific studies were reported on applications such as the measurement of bacterial flagellar thrust using dielectrophoresis [29].

The bulk of the research in dielectrophoresis had been experimental and theoretical, whereas a few numerical approaches such as [22] are also reported.

As already mentioned the particles in an ER suspension in a non-uniform electric field experiences two different electrostatic forces. The first one due to the particle-particle interactions and the second one due to the gradient of the applied electric field. In addition to the above two forces the particles are also subjected to the hydrodynamic force when flow is also involved. The effect of Brownian motion is ignored, as it is appropriate to do so. The two electrostatic forces acting on the particles are in competition with each other, in the sense that the relative importance of the forces determines the structure formation and the separation of the particles and also the time required for reaching steady state. When the particle-particle interaction force is dominating, it results in the formation of inter-particle chains, which in turn delays the process of particle collection in the regions of low or high electric field, whereas when the dielectrophoretic force is dominating, it results in the immediate collection of the particles, without the formation of chains, either at the low or high electric field regions. In a regime where the two electrostatic forces are comparable, particles are seen to form chains, and the chains move collectively to low or high field regions. In all the cases, the particles move along the direction of the dielectrophoretic force to form the stable structure.

The rest of the thesis is organized as follows. In the next chapter the governing equations and the dimensionless parameters that are important in determining the rheological behavior of the ER fluids subjected to uniform and non-uniform electric fields are presented. The numerical method is described in chapter 3 and the results are presented in chapter 4, which show that the particle collection time in a flowing ER fluid subjected to a non-uniform electric field depends on the ratio of the dielectrophoretic and viscous forces, as well as the relative importance of the electrostatic particle-particle interaction force and dielectrophoretic force, and the hydrodynamic force.

CHAPTER 2

GOVERNING EQUATIONS

In this chapter, the electrostatic forces that arise in a non-uniform electric field due to the polarization of particles are described, and the governing, dimensional and dimensionless, equations for both the particles and the fluid are stated. In deriving these equations it is assumed that the particles are spherical, nonconducting and of the same size, whereas the suspending fluid is assumed to be Newtonian and nonconducting.

2.1 Electrostatic Forces

When an ER fluid is subjected to an electric field, the particles become polarized due to the difference between the dielectric constant of the particles and that of the liquid. A polarized particle of the ER fluid experiences an electrostatic force, which can be divided into two parts. The first part is due to the electrostatic interactions among the particles of the ER fluid, and the second part is due to the spatial variation of the electric field.

In the present work, the electrostatic force acting on the particles is approximated by the so-called point-dipole approximation, which assumes that the dipole moment of a particle is not affected by the surrounding particles and that the ratio of particle and fluid permittivities is $O(1)$ (see Refs. [38, 44]). This approximation, however, ignores the secondary redistribution of charges due to the presence of neighboring particles.

For the case where the electric field varies in space, it is assumed that the particle polarization depends on the value of electric field \mathbf{E} at its center. For an isolated spherical particle subjected to an electric field \mathbf{E} , the polarization is given by

$$\mathbf{p} = 4\pi\epsilon_0\epsilon_c\beta a^3\mathbf{E} \quad (2)$$

In order to obtain the interaction force between two particles, the electric field strengths at their centers is considered and are denoted by \mathbf{E}_i and \mathbf{E}_j , respectively. The two particles thus become polarized with dipole moments, $\mathbf{p}_i = 4\pi\epsilon_0\epsilon_c\beta a^3\mathbf{E}_i$ and $\mathbf{p}_j = 4\pi\epsilon_0\epsilon_c\beta a^3\mathbf{E}_j$. Since the direction of \mathbf{E} and its magnitude vary in space, the direction and magnitude of the polarization of the particles also vary in space. It is easy to show that the x-component of the electrostatic interaction force, $\mathbf{F}_{D,ij}$ between particles i and j is:

$$\left(\mathbf{F}_{D,ij} \right)_x = \frac{1}{4\pi\epsilon_0\epsilon_c} \frac{3}{r^5} \left(x_{ij} (3p_{i1}p_{j1} + p_{i2}p_{j2} + p_{i3}p_{j3}) + y_{ij} (p_{i1}p_{j2} + p_{i2}p_{j1}) + z_{ij} (p_{i1}p_{j3} + p_{i3}p_{j1}) \right) - \frac{5}{r^2} x_{ij} (\mathbf{p}_i \cdot \mathbf{r}_{ij})(\mathbf{p}_j \cdot \mathbf{r}_{ij}) \quad (3)$$

Here $\mathbf{r}_{ij} = \mathbf{r}_i - \mathbf{r}_j$, where \mathbf{r}_i and \mathbf{r}_j are the position vectors of particles i and j, r is the magnitude of \mathbf{r}_{ij} , x_{ij} , y_{ij} and z_{ij} are the components of \mathbf{r}_{ij} , p_{i1} , p_{i2} and p_{i3} are the components of \mathbf{p}_i and p_{j1} , p_{j2} and p_{j3} are the components of \mathbf{p}_j . The above expression can be written in vector form as

$$\mathbf{F}_{D,ij} = \frac{1}{4\pi\epsilon_0\epsilon_c} \frac{3}{r^5} \left(\mathbf{r}_{ij} (\mathbf{p}_i \cdot \mathbf{p}_j) + (\mathbf{r}_{ij} \cdot \mathbf{p}_i) \mathbf{p}_j + (\mathbf{r}_{ij} \cdot \mathbf{p}_j) \mathbf{p}_i - \frac{5}{r^2} \mathbf{r}_{ij} (\mathbf{p}_i \cdot \mathbf{r}_{ij})(\mathbf{p}_j \cdot \mathbf{r}_{ij}) \right) \quad (4)$$

It is easy to show that in a spatially uniform electric field the above expression takes the following well-known form in spherical coordinates,

$$\mathbf{F}_{D,ij}(r_{ij}, \theta_{ij}) = f_0 \left(\frac{a}{r_{ij}} \right)^4 \left((3 \cos^2 \theta_{ij} - 1) \hat{\mathbf{e}}_r + \sin 2\theta_{ij} \hat{\mathbf{e}}_\theta \right) \quad (5)$$

where $f_0 = 12\pi\epsilon_0\epsilon_c a^2\beta^2 E_0^2$, E_0 being the magnitude of the uniform electric field along the z-axis, and θ_{ij} denotes the angle between the z-axis and the position vector \mathbf{r}_{ij} .

The net electrostatic interaction force acting on the i^{th} particle is the sum of the interaction forces with all other particles of the suspension:

$$\mathbf{F}_{D,i} = \sum_{i=1, i \neq j}^N \mathbf{F}_{D,ij} \quad (6)$$

where N is the number of particles. Also, it is interesting to notice from Equation (5) that the magnitude of the dipole-dipole interaction force is inversely proportional to the fourth power of the distance between the particles. It thus decreases rapidly with increasing $|\mathbf{r}_{ij}|$ and can be ignored when the distance between two particles is much larger than the particle diameter.

In addition to the above dipole-dipole interaction force, the i^{th} particle is also subjected to a force at its center, due to the gradient of \mathbf{E} , which can be recalled, is given by $\mathbf{F}_{\text{DEP},i} = 4\pi a^3 \epsilon_0 \epsilon_c \beta \mathbf{E}_i \cdot \nabla \mathbf{E}_i$. The total electrostatic force $\mathbf{F}_{E,i}$ acting on the i^{th} particle is given by the sum of the above two forces,

$$\mathbf{F}_{E,i} = \mathbf{F}_{\text{DEP},i} + \mathbf{F}_{D,i} \quad (7)$$

To calculate the electric field \mathbf{E} , the electric potential problem $\nabla^2 \phi = 0$, is solved first, then subjected to prescribed boundary conditions, and then calculate $\mathbf{E} = \nabla \phi$.

2.2 Governing Equations for the Fluid and the Particles

Consider the domain containing a Newtonian fluid and N solid particles denoted by Ω , Let the interior of the i^{th} particle be $P_i(t)$, and the domain boundary be Γ . The governing equations for the fluid-particle system are:

$$\begin{aligned} \rho_L \left(\frac{\partial \mathbf{u}}{\partial t} + \mathbf{u} \cdot \nabla \mathbf{u} \right) &= -\nabla p + \nabla \cdot (2\eta \mathbf{D}) && \text{in } \Omega \setminus \overline{P(t)} \\ \nabla \cdot \mathbf{u} &= 0 && \text{in } \Omega \setminus \overline{P(t)} \\ \mathbf{u} &= \mathbf{u}_L && \text{on } \Gamma \\ \mathbf{u} &= \mathbf{U}_i + \boldsymbol{\omega}_i \times \mathbf{r}_i && \text{on } \partial P_i(t) \quad i=1, \dots, N \end{aligned} \quad (8)$$

Here \mathbf{u} is the fluid velocity, p is the pressure, η is the dynamic viscosity of the fluid, ρ_L is the density of the fluid, \mathbf{D} is the symmetric part of the velocity gradient tensor and \mathbf{U}_i and $\boldsymbol{\omega}_i$ are the linear and angular velocities of the i^{th} particle. The above equations are solved using the following initial conditions $\mathbf{u}|_{t=0} = \mathbf{u}_0$, where \mathbf{u}_0 is the known initial value of the velocity.

The linear velocity \mathbf{U}_i and angular velocity $\boldsymbol{\omega}_i$ of the i^{th} particle are governed by

$$m_i \frac{d\mathbf{U}_i}{dt} = \mathbf{F}_i + \mathbf{F}_{E,i} \quad (10)$$

$$I_i \frac{d\boldsymbol{\omega}_i}{dt} = \mathbf{T}_i \quad (11)$$

$$\mathbf{U}_i|_{t=0} = \mathbf{U}_{i,0} \quad (12)$$

$$\boldsymbol{\omega}_i|_{t=0} = \boldsymbol{\omega}_{i,0} \quad (13)$$

where m_i and I_i are the mass and moment of inertia of the i^{th} particle, \mathbf{F}_i and \mathbf{T}_i are the hydrodynamic force and torque acting on the i^{th} particle and $\mathbf{F}_{E,i} = \mathbf{F}_{\text{DEP},i} + \mathbf{F}_{\text{D},i}$ is the net electrostatic force acting on the i^{th} particle. As mentioned above, in this work, only spherical particles are considered, and therefore it is not required to keep track of the particle orientation. The particle positions are obtained from

$$\frac{d\mathbf{X}_i}{dt} = \mathbf{U}_i \quad (14)$$

$$\mathbf{X}_i|_{t=0} = \mathbf{X}_{i,0} \quad (15)$$

where $\mathbf{X}_{i,0}$ is the position of the i^{th} particle at time $t = 0$. In this work, as already mentioned, it is assumed that all particles have the same properties and hence the same density ρ_p , and since they have the same radius, they also have the same mass, m .

2.3 Dimensionless Parameters

The above equations are nondimensionalized by assuming that the characteristic length, velocity, time, stress, angular velocity and electric field scales are a , \mathbf{U} , a/\mathbf{U} , $\eta\mathbf{U}/a$, \mathbf{U}/a and E_0 , respectively. The gradient of the electric field is assumed to scale as E_0/L , where L is the distance between the electrodes, which for our simulations is of the same order of magnitude as the domain width. The non-dimensional equations, after using the same symbols for the dimensionless variables for the fluid and the particle linear and angular momentums, are:

$$\begin{aligned} \text{Re} \left(\frac{\partial \mathbf{u}}{\partial t} + \mathbf{u} \cdot \nabla \mathbf{u} \right) &= -\nabla p + \nabla \cdot \boldsymbol{\sigma} && \text{in } \Omega \setminus \overline{P(t)} \\ \nabla \cdot \mathbf{u} &= 0 && \text{in } \Omega \setminus \overline{P(t)} \end{aligned} \quad (16)$$

$$\frac{d\mathbf{U}}{dt} = \frac{6\pi\eta a^2}{m\mathbf{U}} \int \left(\frac{-p\mathbf{I} + \boldsymbol{\sigma}}{6\pi} \right) \cdot \mathbf{n} ds + \frac{4\pi a^4 \epsilon_0 \epsilon_c \beta |E_0|^2}{m\mathbf{U}^2 L} (\mathbf{E} \cdot \nabla \mathbf{E}) + \frac{3\pi \epsilon_0 \epsilon_c a^3 \beta^2 |E_0|^2}{4m\mathbf{U}^2 |r_{ij}|^4} (\mathbf{F}_D) \quad (17)$$

$$\frac{d\boldsymbol{\omega}}{dt} = \frac{5\eta a^2}{2m\mathbf{U}} \int (\mathbf{x} - \mathbf{X}) [(-p\mathbf{I} + \boldsymbol{\sigma}) \cdot \mathbf{n}] ds \quad (18)$$

Notice that a factor of 6π is introduced in the first term on the right hand side of (15) to ensure that in the Stokes flow limit the quantity inside the integral, for an isolated particle, is equal to one. The above equations contain the following dimensionless

$$\text{parameters: } \text{Re} = \frac{\rho_L \mathbf{U} a}{\eta}, \quad P_1 = \frac{6\pi\eta a^2}{m\mathbf{U}}, \quad P_2 = \frac{3\pi\epsilon_0\epsilon_c\beta^2 a^3 |E_0|^2}{4m\mathbf{U}^2}, \quad P_3 = \frac{4\pi\epsilon_0\epsilon_c\beta a^4 |E_0|^2}{m\mathbf{U}^2 L} \quad \text{and}$$

$h' = \frac{L}{a}$. Here Re is the Reynolds number, which determines the relative importance of the

fluid inertia and viscous forces, P_1 is the ratio of the viscous and inertia forces, P_2 is the ratio of the electrostatic particle-particle interaction and inertia forces and P_3 is the ratio of the dielectrophoretic and inertia forces. Another important parameter, which does not appear directly in the above equations, is the solids fraction. The rheological properties of

ER suspensions depend strongly on the solids fraction of the particles. Another Reynolds

number $\text{Re}_L = \frac{\rho_L L \mathbf{U}}{\eta}$ can be defined based on the channel width L and another parameter

$P_4 = \frac{P_2}{P_3} = \frac{3\beta L}{16a}$ can also be defined, which determines the relative importance of the

particle-particle interaction and dielectrophoretic forces. Notice that P_4 depends on the ratio of the domain size and the particle radius, as the spatial gradient of the electric field depends on the domain size and the particle-particle interaction force depends on the distance between the particles.

When the particle and fluid inertia are negligible, i.e., the particle and fluid inertial terms can be set to zero, the number of dimensionless parameters reduces by two.

The dimensionless parameters in this case are the Mason number,

$Ma = \frac{P_1}{P_2} = \frac{8\eta U}{\epsilon_0 \epsilon_c \beta^2 a |E_0|^2}$, and $P_5 = \frac{P_3}{P_1} = \frac{2\epsilon_0 \epsilon_c \beta a^2 |E_0|^2}{3\eta UL}$. The Mason number determines

the relative importance of the viscous force and the electrostatic particle-particle interaction force, and P_5 determines the relative importance of the electrostatic dielectrophoretic and viscous forces.

For the pressure driven flows of ER suspensions, the characteristic velocity is assumed to be the center line velocity of the parabolic flow, undisturbed by the particles,

in a two dimensional channel of the same height, i.e., $U = \frac{L^2}{8\eta} \frac{dp}{dx}$, where L is the channel

height and $\frac{dp}{dx}$ is the applied pressure gradient. This is appropriate because for our

simulations the channel width is larger than the channel height. For the cases where the

imposed pressure gradient is zero, the characteristic velocity $U = \frac{2\epsilon_0 \epsilon_c \beta a^2 |E_0|^2}{3\eta L}$, which

is obtained by assuming that the dielectrophoretic force and the viscous drag terms

balance each other. For this choice of the characteristic velocity, however, the

dimensionless parameters P_1 and P_3 are equal and thus P_5 reduces to one. It is worth

noting that this velocity also determines the time scale in which the particles collect in the

low or high electric field regions.

CHAPTER 3

FINITE ELEMENT METHOD

3.1 the Computational Scheme

The computational scheme used in this paper is a generalization of the DLM finite-element scheme described in [18, 49]. In this scheme, the fluid flow equations are solved on the combined fluid-solid domain, and the motion inside the particle boundaries is forced to be rigid-body motion using a distributed Lagrange multiplier. The fluid and particle equations of motion are combined into a single combined weak equation of motion, eliminating the hydrodynamic forces and torques, which helps ensure the stability of the time integration. For the sake of simplicity, in this chapter, it is assumed that there is only one particle. The extension to the multi-particle case is straightforward.

The solution and variation are required to satisfy the strong form of the constraint of rigid body motion throughout $P(t)$. In the distributed Lagrange multiplier method, this constraint is removed from the velocity space and enforced weakly as a side constraint using a distributed Lagrange multiplier term. It was shown in [18, 49] that the following weak formulation of the problem holds in the extended domain:

For a.e. $t > 0$, find $\mathbf{u} \in \overline{W}_{\mathbf{u}\Gamma}$, $p \in L^2_0(\Omega)$, $\lambda \in \Lambda(t)$, $\mathbf{U} \in \mathbf{R}^3$ and $\boldsymbol{\omega} \in \mathbf{R}^3$, satisfying

$$\begin{aligned} & \int_{\Omega} \rho_L \left(\frac{d\mathbf{u}}{dt} - \mathbf{g} \right) \cdot \mathbf{v} dx - \int_{\Omega} p \nabla \cdot \mathbf{v} dx + \int_{\Omega} 2\eta \mathbf{D}[\mathbf{u}] : \mathbf{D}[\mathbf{v}] dx \\ & + \left(1 - \frac{\rho_L}{\rho_d} \right) \left(M \left(\frac{d\mathbf{U}}{dt} - \mathbf{g} \right) \cdot \mathbf{V} + I \frac{d\boldsymbol{\omega}}{dt} \cdot \boldsymbol{\xi} \right) - \mathbf{F}' \cdot \mathbf{V} = \langle \boldsymbol{\lambda}, \mathbf{v} - (\mathbf{V} + \boldsymbol{\xi} \times \mathbf{r}) \rangle_{P(t)} \\ & \text{for all } \mathbf{v} \in \overline{W}_0, \mathbf{V} \in \mathbf{R}^3, \text{ and } \boldsymbol{\xi} \in \mathbf{R}^3, \end{aligned} \quad (19)$$

$$\int_{\Omega} q \nabla \cdot \mathbf{u} dx = 0 \quad \text{for all } q \in L^2(\Omega), \quad (20)$$

$$\langle \boldsymbol{\mu}, \mathbf{u} - (\mathbf{U} + \boldsymbol{\omega} \times \mathbf{r}) \rangle_{P(t)} = 0 \quad \text{for all } \boldsymbol{\mu} \in \Lambda(t), \quad (21)$$

$$\mathbf{u}|_{t=0} = \mathbf{u}_o \quad \text{in } \Omega, \quad (22)$$

as well as the kinematic equations and the initial conditions for the particle linear and angular velocities. Here \mathbf{F}' is the additional body force applied to the particles to limit the extent of overlap (see Equation (19) in Glowinski, et al. (1999) and λ is the distributed Lagrange multiplier

$$\begin{aligned} \overline{W}_{u\Gamma} &= \{ \mathbf{v} \in H^1(\Omega)^3 \mid \mathbf{v} = \mathbf{u}_\Gamma(t) \text{ on } \Gamma \}, \\ \overline{W}_0 &= H_0^1(\Omega)^3, \\ L_0^2(\Omega) &= \{ q \in L^2(\Omega) \mid \int_\Omega q \, dx = 0 \}, \end{aligned} \quad (23)$$

and $\Lambda(t)$ is $L^2(P(t))^3$, with $\langle \cdot, \cdot \rangle_{P(t)}$ denoting the L^2 inner product over the particle, where Γ^- is the upstream part of Γ . In our simulations, since the velocity and $\boldsymbol{\mu}$ are in L^2 , the following inner product will be used.

$$\langle \boldsymbol{\mu}, \mathbf{v} \rangle_{P(t)} = \int_{P(t)} (\boldsymbol{\mu} \cdot \mathbf{v}) \, dx. \quad (24)$$

In order to solve the above problem numerically, the domain will be discretized using a regular tetrahedral mesh T_h for the velocity, where h is the mesh size, and a regular tetrahedral mesh T_{2h} for the pressure. The following finite dimensional spaces are defined for approximating $\overline{W}_{u\Gamma}$, \overline{W}_0 , $L^2(\Omega)$ and $L_0^2(\Omega)$:

$$\begin{aligned} W_{u\Gamma,h} &= \{ \mathbf{v}_h \in C^0(\overline{\Omega})^3 \mid \mathbf{v}_h|_T \in P_1 \times P_1 \times P_1 \text{ for all } T \in T_h, \mathbf{v}_h = \mathbf{u}_{\Gamma,h} \text{ on } \Gamma \}, \\ W_{0,h} &= \{ \mathbf{v}_h \in C^0(\overline{\Omega})^3 \mid \mathbf{v}_h|_T \in P_1 \times P_1 \times P_1 \text{ for all } T \in T_h, \mathbf{v}_h = 0 \text{ on } \Gamma \}, \\ L_h^2 &= \{ q_h \in C^0(\overline{\Omega}) \mid q_h|_T \in P_1 \text{ for all } T \in T_{2h} \}, \end{aligned} \quad (25)$$

$$L_{0,h}^2 = \{q_h \in L_h^2 \mid \int_{\Omega} q_h \, d\mathbf{x} = 0\}, \quad (26)$$

The particle inner product terms in (19) and (21) are obtained using the discrete L^2 inner product defined in Glowinski, et al. (1999). Specifically, M points are chosen, $\mathbf{x}_1, \dots, \mathbf{x}_M$ that uniformly cover $\bar{P}(t)$, and define

$$\Lambda_h(t) = \left\{ \boldsymbol{\mu}_h \mid \boldsymbol{\mu} = \sum_{i=1}^M \boldsymbol{\mu}_{h,i} \delta(\mathbf{x} - \mathbf{x}_i), \quad \boldsymbol{\mu}_{h,1}, \dots, \boldsymbol{\mu}_{h,M} \in \mathbf{R}^3 \right\}.$$

Using these finite dimensional spaces, it is straightforward to discretize Equations 19-22.

3.2 Collision strategy

In the finite element simulation technique used, the particle overlap is prevented by imposing a repulsive force. In simulations, the repulsive force is assumed to be large enough so that the overlap between the particles and the walls is smaller than one hundredth of the velocity element size. The additional body force—which is repulsive in nature—is added to Equation (10). The particle-particle repulsive force is given by

$$\mathbf{F}_{ij}^R = \begin{cases} 0 & \text{for } r_{ij} > D \\ k(\mathbf{r}_i - \mathbf{r}_j)(D - r_{i,j}), & \text{for } r_{ij} < D \end{cases} \quad (27)$$

where r_{ij} is the distance between the centers of the i^{th} and j^{th} particles, \mathbf{r}_i and \mathbf{r}_j are the position vectors of the particle centers, and k is the stiffness parameter. The repulsive force between the particles and the wall is given by

$$\mathbf{F}_{ij}^W = \begin{cases} 0 & \text{for } r_i > D \\ k_w(\mathbf{r}_i - \mathbf{r}_j)(D - r_i), & \text{for } r_i < D \end{cases} \quad (28)$$

where r_i is the distance between the centers of the i^{th} particle and the imaginary particle on the other side of the wall Γ_j , and k_w is the stiffness parameter for particle wall collision. The above particle-particle repulsive forces and the particle-wall repulsive forces are added to Equation (10) to obtain

$$m_i \frac{dU_i}{dt} = F_i + F_{E,i} + F'_{E,i}$$

where

$$F'_{E,i} = \sum_{\substack{j=1 \\ j \neq i}}^N F_{i,j}^R + \sum_{j=1}^4 F_{i,j}^W \quad (29)$$

is the repulsive force exerted on the i^{th} particle by the other particles and the walls. The repulsive force acts only when the particles overlap each other.

3.3 Time Discretization Using the Marchuk-Yanenko Operator Splitting Scheme

The initial value problem (19-22) is solved by using the Marchuk-Yanenko operator-splitting scheme, which allows us to decouple its three primary difficulties:

1. The incompressibility condition, and the related unknown pressure p_h ,
2. The nonlinear advection term,
3. The constraint of rigid-body motion in $P_h(t)$, and the related distributed Lagrange multiplier λ_h .

The Marchuk-Yanenko operator-splitting scheme can be applied to an initial value problem of the form

$$\frac{d\phi}{dt} + A_1(\phi) + A_2(\phi) + A_3(\phi) = f$$

where the operators A_1 , A_2 and A_3 can be multi-valued. Let Δt be the time step. The following version of the Marchuk-Yanenko operator splitting scheme is used to simulate the motion of particles in an ER fluid:

Set $\mathbf{u}^0 = \mathbf{u}_{0,h}$, $\mathbf{U}^0 = \mathbf{U}_0$, $\mathbf{X}^0 = \mathbf{X}_0$ and $\omega^0 = \omega_0$, and calculate \mathbf{E} by solving $\nabla^2 \phi = 0$, subjected to the electric potential boundary conditions, and then calculating $\mathbf{E} = \nabla \phi$.

For $n = 0, 1, 2, \dots$ assuming \mathbf{u}^n , \mathbf{U}^n , \mathbf{X}^n , and ω^n are known, the values for the $(n+1)^{\text{th}}$ time step are found using the following steps:

STEP 1:

Find $\mathbf{u}^{n+1/4} \in W_{\text{u},h}^{n+1}$ and $p^{n+1/4} \in L_{0,h}^2$, by solving

$$\int_{\Omega} \rho_L \frac{\mathbf{u}^{n+1/4} - \mathbf{u}^n}{\Delta t} \cdot \mathbf{v} \, dx - \int_{\Omega} p^{n+1/4} \nabla \cdot \mathbf{v} \, dx + \alpha \int_{\Omega} 2\eta_s \mathbf{D}[\mathbf{u}^{n+1/4}] : \mathbf{D}[\mathbf{v}] \, dx = 0$$

for all $\mathbf{v} \in W_{0,h}$,

$$\int_{\Omega} q \nabla \cdot \mathbf{u}^{n+1/4} \, dx = 0 \quad \text{for all } q \in L_h^2, \quad (30)$$

STEP 2:

Find $\mathbf{u}^{n+2/4} \in W_{\text{u},h}^{n+1}$, by solving

$$\int_{\Omega} \rho_L \frac{\mathbf{u}^{n+2/4} - \mathbf{u}^{n+1/4}}{\Delta t} \cdot \mathbf{v} \, dx + \int_{\Omega} \rho_L (\mathbf{u}^{n+2/4} \cdot \nabla \mathbf{u}^{n+2/4}) \cdot \mathbf{v} \, dx + \beta \int_{\Omega} 2\eta_s \mathbf{D}[\mathbf{u}^{n+2/4}] : \mathbf{D}[\mathbf{v}] \, dx = 0$$

for all $\mathbf{v} \in W_{0,h}$ (31)

STEP 3:

Compute $\mathbf{U}^{n+2/4}$ and $\mathbf{X}^{n+2/4}$ using the prediction procedure

Set $\mathbf{U}^{n,0} = \mathbf{U}^n$, $\mathbf{X}^{n,0} = \mathbf{X}^n$.

Do $k = 1, K$

Calculate $\mathbf{F}_E(\mathbf{X}^{n,k-1})$

$$\mathbf{U}^{*n,k} = \mathbf{U}^{n,k-1} + \left(\mathbf{g} + \left(1 - \frac{\rho_L}{\rho_d} \right)^{-1} \mathbf{M}^{-1} \left[\mathbf{F}'(\mathbf{X}^{n,k-1}) + \mathbf{F}_E(\mathbf{X}^{n,k-1}) \right] \right) \frac{\Delta t}{\mathbf{K}}$$

$$\mathbf{X}^{*n,k} = \mathbf{X}^{n,k-1} + \left(\frac{\mathbf{U}^{n,k-1} + \mathbf{U}^{*n,k}}{2} \right) \frac{\Delta t}{\mathbf{K}}$$

$$\mathbf{U}^{n,k} = \mathbf{U}^{*n,k}$$

$$+ \left(\mathbf{g} + \left(1 - \frac{\rho_L}{\rho_d} \right)^{-1} \mathbf{M}^{-1} \frac{\mathbf{F}'(\mathbf{X}^{n,k-1}) + \mathbf{F}'(\mathbf{X}^{*n,k-1}) + \mathbf{F}_E(\mathbf{X}^{n,k-1}) + \mathbf{F}_E(\mathbf{X}^{*n,k-1})}{2} \right) \frac{\Delta t}{\mathbf{K}}$$

$$\mathbf{X}^{n,k} = \mathbf{X}^{n,k-1} + \left(\frac{\mathbf{U}^{n,k-1} + \mathbf{U}^{n,k}}{2} \right) \frac{\Delta t}{\mathbf{K}}$$

end do

$$\text{Then set } \mathbf{U}^{n+2/4} = \mathbf{U}^{n,K}, \mathbf{X}^{n+2/4} = \mathbf{X}^{n,K}. \quad (32)$$

The next step consists of finding $\mathbf{u}^{n+1} \in \mathbf{W}_{\text{u}\Gamma, h}^{n+1}$, $\boldsymbol{\lambda}^{n+1} \in \Lambda_h((n+2/4)\Delta t)$, $\mathbf{U}^{n+1} \in \mathbf{R}^3$, and $\boldsymbol{\omega}^{n+1} \in \mathbf{R}^3$, satisfying

$$\begin{aligned} & \int_{\Omega} \rho_L \frac{\mathbf{u}^{n+1} - \mathbf{u}^{n+2/4}}{\Delta t} \cdot \mathbf{v} \, d\mathbf{x} + \left(1 - \frac{\rho_L}{\rho_d} \right) \left(\mathbf{M} \frac{\mathbf{U}^{n+1} - \mathbf{U}^{n+2/4}}{\Delta t} \cdot \mathbf{V} + \mathbf{I} \frac{\boldsymbol{\omega}^{n+1} - \boldsymbol{\omega}^{n+2/4}}{\Delta t} \cdot \boldsymbol{\xi} \right) + \\ & = \left\langle \boldsymbol{\lambda}^{n+1}, \mathbf{v} - (\mathbf{V} + \boldsymbol{\xi} \times \mathbf{r}^{n+2/4}) \right\rangle_{P((n+2/4)\Delta t)} \end{aligned}$$

$$\text{for all } \mathbf{v} \in \mathbf{W}_{0,h}, \mathbf{V} \in \mathbf{R}^2, \text{ and } \boldsymbol{\xi} \in \mathbf{R} \quad (33)$$

where the center of the particle $P((n+2/4)\Delta t)$ is at the location $\mathbf{X}^{n+2/4}$.

Then set $\mathbf{X}^{n+1,0} = \mathbf{X}^n$.

For $k = 1, K$, follow the do-loop

$$\mathbf{X}^{*n+1,k} = \mathbf{X}^{n+1,k-1} + \left(\frac{\mathbf{U}^n + \mathbf{U}^{n+1}}{2} \right) \frac{\Delta t}{\mathbf{K}}$$

$$\mathbf{X}^{n,k} = \mathbf{X}^{*n,k-1} + \left(1 - \frac{\rho_L}{\rho_d}\right)^{-1} \mathbf{M}^{-1} \left(\frac{\mathbf{F}'(\mathbf{X}^{n+1,k-1}) + \mathbf{F}'(\mathbf{X}^{*n+1,k})}{2} \right) \frac{(\Delta t)^2}{2K}$$

end do

$$\text{Then set } \mathbf{X}^{n+1} = \mathbf{X}^{n+1,K}. \quad (34)$$

Then set $\mathbf{p}^{n+1} = \mathbf{p}^{n+1/4}$, and go back to the first step.

Remarks:

1. The problems arising in the first and second steps are solved using the conjugate gradient algorithm described in [18].
2. In this work, it is assumed that $\alpha_1 = 0.5$ and $\alpha_2 = 0.5$.
3. The third step is used to obtain the distributed Lagrange multiplier that enforces rigid body motion inside the particles. This problem is solved by using the conjugate gradient method described in [18, 49]. In this step, the electrostatic forces that arise due to the dielectrophoretic effect and the dipole-dipole interactions, are accounted for.

CHAPTER 4

NUMERICAL RESULTS

In this chapter, the numerical results obtained, using the algorithm discussed, for the motion of the particles of ER suspensions subjected to spatially uniform and spatially varying electric fields are discussed. Figure 4.1.a shows a typical domain used in our simulations, as well as an initial periodic arrangement of the particles and the coordinate system. The fluid velocity is assumed to be zero on the sidewalls of the domain and periodic along the z-direction. The electric field is also assumed to be periodic in the z-direction. The electrostatic and hydrodynamic forces include contributions from the periodic images of particles in the z-direction. The pressure gradient along the z-direction of the channel will be denoted by dp/dz and the x-, y- and z-components of the fluid velocity are referred to as u , v and w , respectively.

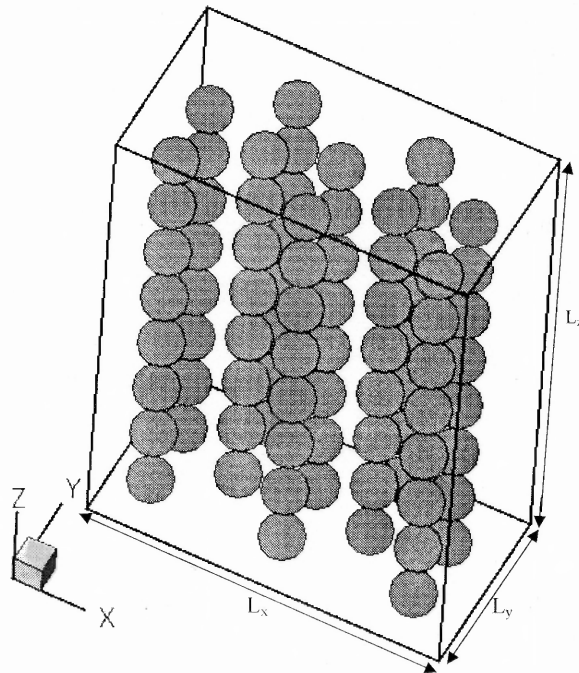


Figure 4.1.a An oblique view of a typical domain used for simulations.

The uniform electric field is generated by placing electrodes on the sidewalls parallel to the y - z plane. In the case of non-uniform electric field, the field is generated by placing one or two pairs of electrodes on the domain sidewalls parallel to the yz -coordinate plane. In order to generate a non-uniform electric field the electrodes are made shorter than the sidewalls so that they do not cover the sidewalls entirely. The electrodes are so placed that they do not affect the fluid boundary conditions, by embedding them into the sidewalls. The generated non-uniform electric fields vary at scales comparable to the domain size since the electrodes are separated by distances that are comparable to the length of the electrodes. The width of the electrodes in the y -direction is equal to the domain width and hence the electric field does not vary in the y -direction. The fluid and particle velocities, and particle-particle interaction forces, however, vary in the y -direction.

Throughout this work, it is assumed that the dynamic fluid viscosity $\eta = 0.01$ poise and the particle diameter and density are 0.2 mm and 1.01 g/cm³, respectively. The fluid density is $\rho_L = 1.0$ g/cm³. The gravity is ignored, as the density of particles is quite close to that of the fluid and the particle diameter is small. For most cases presented in this paper, the dielectric constant of the particles is assumed to be 7.3, and that of the fluid is assumed to be 23.3. The initial fluid and particle velocities are set to zero. The domain is discretized using a regular pseudo P2-P1 tetrahedral mesh, as described in the previous chapter.

The result chapter is divided into two. The behavior of the ER fluid in a spatially uniform electric field is studied and the results are reported for the same in the first

subsection. Next, the ER fluid is subjected to a non-uniform electric field and the results obtained for various cases are reported in the second subsection.

4.1 Uniform Electric Field

4.1.1 Convergence

To show that the results converge with mesh and time step refinements for uniform electric fields, the motion of three particles in a pressure driven flow and subjected to a uniform electric field along the x-direction is considered. The magnitude of applied electric field strength is 3×10^3 and the pressure gradient is 20. At $t = 0$, the three particles are placed on a straight line parallel to the x-axis as shown in Figure 4.1.1.a. The middle particle is placed at the center of channel cross-section and the other two particles are placed at a distance of 0.3 mm above and below the cross-section center. The initial particle and fluid velocities are assumed to be zero. The channel dimensions are (1 mm x 1 mm x 2.4 mm).

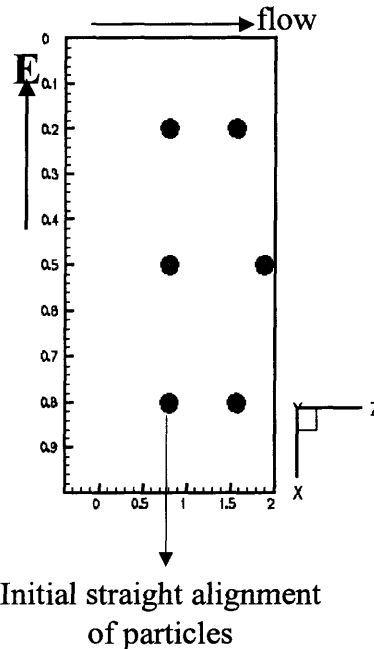


Figure 4.1.1.a The initial arrangement of particles for the convergence study. In pressure driven flows the chains get bend as shown.
Note: The figure shown is not to scale

To show that the results converge with time-step refinement, a uniform tetrahedral mesh with 19,200 elements is used. In a tetrahedral element there are six velocity and four pressure nodes. The size of velocity elements in this case is $1/48$. Time steps of 5×10^{-4} , 2.5×10^{-4} and 1.25×10^{-4} are used to study convergence with the size of time step.

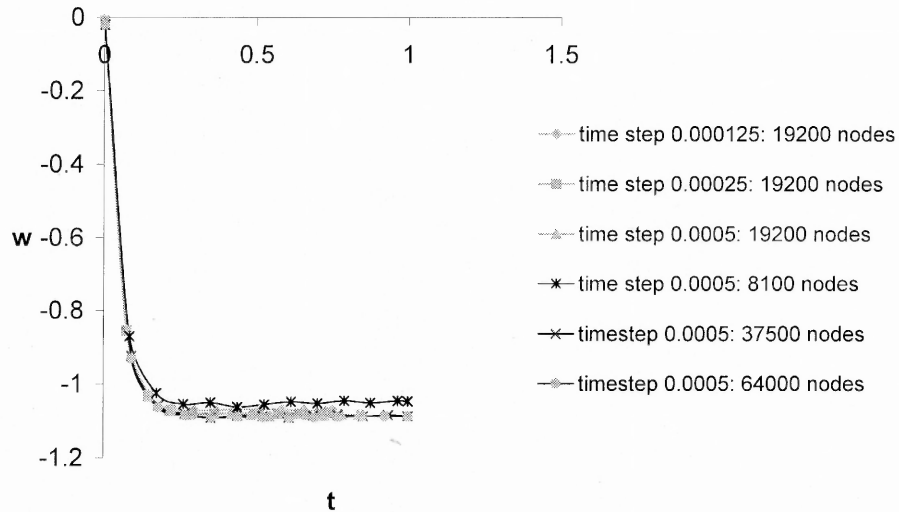


Figure 4.1.1.b The z-component of velocity w for the middle particle is shown for different values of time step and mesh size.

The z-component of velocity for the middle particle is plotted as a function of time in Figure 4.1.1.b. The figure shows that the particle accelerates in the z-direction due to the hydrodynamic forces and reaches a constant velocity at $t \approx 0.3$ s. The trajectories for the three different values of the time step shown in this plot are virtually identical. It may therefore be concluded that the results are independent of the time steps used.

In order to show that the results also converge with mesh refinement, similar simulations are performed for three regular tetrahedral meshes. The size of the velocity elements for the first mesh was $1/36$, for the second mesh $1/60$ and for the third mesh $1/72$. The number of elements in the first mesh was 8,100, second mesh 37,500 and in the third mesh 64,800. The time step for these simulations was 5×10^{-4} . From Figure 4.1.1.c it can be seen that the trajectory of middle particle is approximately the same for the second and third meshes, and therefore it may be concluded that the results are also independent of mesh resolution.

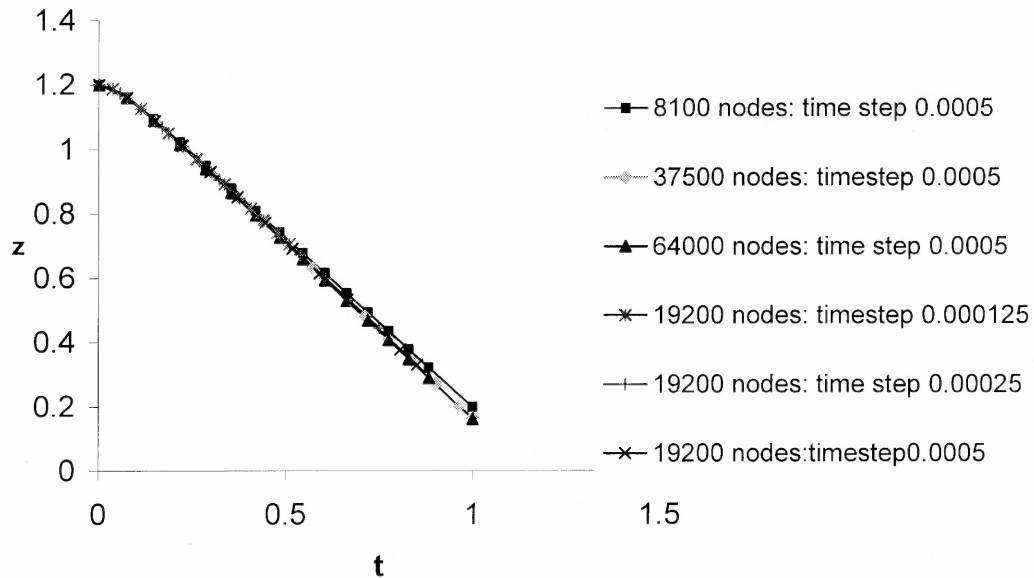


Figure 4.1.1.c The z-coordinate of middle particle is plotted for different values of time step and mesh size.

4.1.2 Effect of Hydrodynamic and Electrostatic Forces on ER Liquids

When a channel containing an ER liquid is subjected to a uniform electric field along the channel cross section the electrostatic forces acting on the particles tend to form chains parallel to the field direction. In a pressure driven flow, on the other hand, since the velocity profile is parabolic, the flow tends to bend and break the chains. Clearly, when

the magnitude of the electrostatic force is much larger than that of the hydrodynamic force the chains are stable but the chains break when the hydrodynamic force dominates. When the two forces are of comparable magnitudes the chains are stable but arch shaped. In this chapter this phenomenon is investigated and it is shown that the degree of bending is determined by the relative magnitudes of electrostatic and hydrodynamic forces.

In order to study formation of chains when both electrostatic and hydrodynamic forces are acting on the particles, the case of a chain formed with three particles in a pressure driven flow is considered. A pressure gradient of 20 is applied to a domain with dimensions 1 mm x 1 mm x 2.4 mm in the x-, y- and z-directions. The electric field is applied along x-direction and its strength is assumed to be 3×10^2 , 6×10^2 , 1×10^3 and 3×10^3 . The particles are initially placed at 0.2 mm, 0.5 mm and 0.8 mm along a line parallel to the x-axis.

As expected, the particle at the channel center moves faster compared to the other two, as the velocity profile is approximately parabolic. The velocity profile is not exactly parabolic because of the presence of the particles. The electrostatic forces, on the other hand, tend to align particles in a chain parallel to the electric field direction. The combined effect of these two forces results in an arch shaped particle chain. The degree of bending for the four cases is different. For $|\mathbf{E}|=3 \times 10^2$, the smallest value of the electric field considered, the hydrodynamic forces overpower the electrostatic forces and the chain bends significantly as can be observed from Figure 4.1.2.a In fact, in this case the

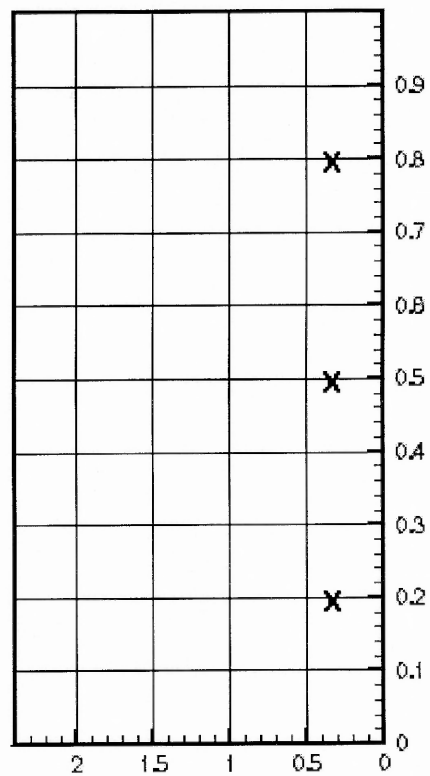
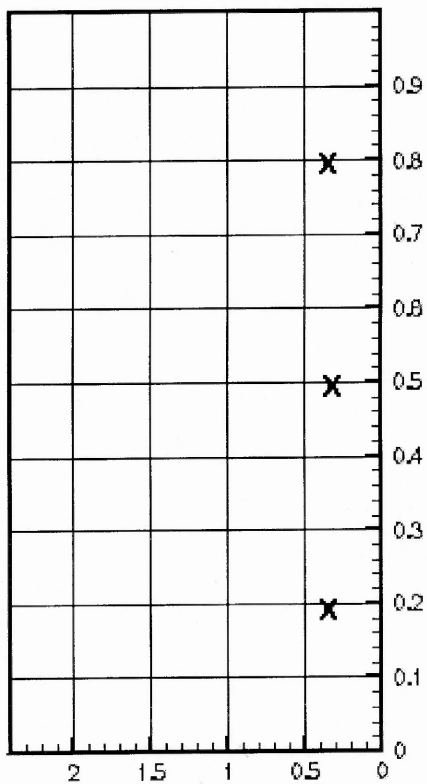
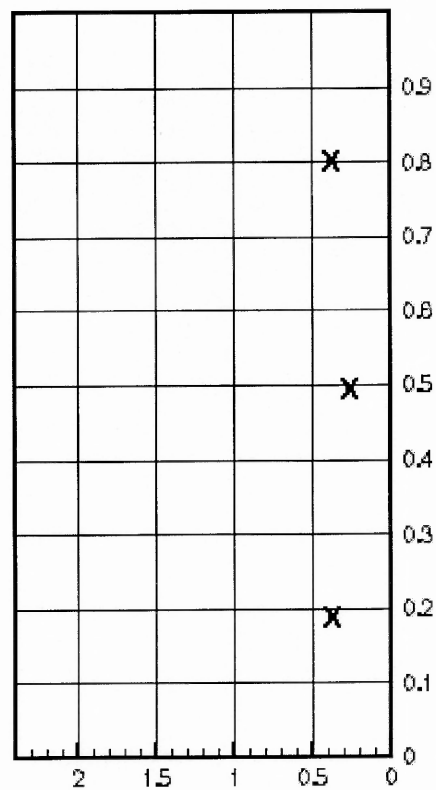
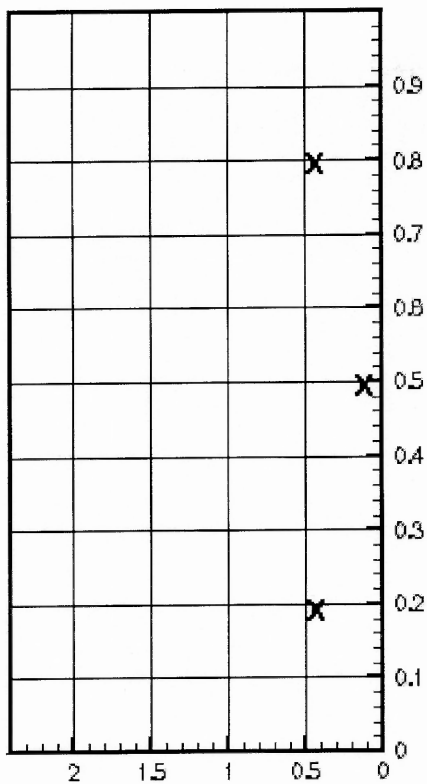


Figure 4.1.2 Electric field strength, a. 3×10^2 , b. 6×10^2 , c. 1×10^3 , d. 3×10^3
 Note: Particle positions are shown by x.

chain is still bending at $t = 0.75$ s. But, as the electric field strength is increased, the bending angle decreases, as can be seen from Figures. 4.1.2.b and 4.1.2.c for which the electric field strengths are 6×10^2 and 1×10^3 , respectively. Finally, when the electric field strength is 3×10^3 the electrostatic forces are much larger than the hydrodynamic forces and the chain remains approximately straight (see Figure 4.1.2.d).

4.1.3 Time Evolution of Particle-Scale Structure Under No Imposed Flow

The interaction among particles is much more complex when the particle concentration is not small, as the particle chains cannot move freely without colliding with the other particle chains. To study this the motion of 105 particles placed in a box with sides 1.6 mm x 1 mm x 2.1 mm along the x- y- and z-directions, is considered. Initially, the particles are placed on a staggered periodic lattice as shown in Figure 4.1.3.a. A uniform electric field of strength 3×10^3 is applied along the x-direction and the pressure gradient is assumed to be zero.

Simulations show that irregular chains, approximately parallel to the direction of electric field, begin to form at $t = 0.035$ s (Figure 4.1.3.b), and by $t = 0.08$ s they become more organized, as can be seen from Figure 4.1.3.c and Figure 4.1.3.d. Simulations also show that the particles move rather rapidly initially during which the nearest neighbors become aligned with the electric field direction. The magnitude of electrostatic forces is the largest during this stage, as it varies inversely with the fourth power of the distance between the particles and the distance between the nearest neighbors is the smallest. After the nearest neighbors become aligned with the electric field, the particles farther away from each other begin to align and form chains. This process however progresses at a

much slower pace, as the electrostatic forces driving it are relatively smaller in magnitude. Once the particles align themselves in chains parallel to the electric field direction, there is no appreciable change in the particle scale structure and the particles tend to maintain their positions in their respective chains till time $t = 0.15$ s.

From equation (5) in chapter 2 it is quite obvious that the force exerted by a particle on its adjacent one is either attractive or repulsive depending on the angle between them. When the angle between the two particles, θ_{ij} is such that the particles are perpendicular to each other, the force is purely repulsive, and the force is completely attractive when the particles are parallel to each other. This results in a torque, which rotates the particles in the xy plane in an effort to bring the particles parallel to each other. This can be clearly observed from Figures 4.1.3.e-4.1.3.g. Figure 4.1.3.e shows the initial random position of the particles, while Figure 4.1.3.f shows the straight chains formed and the oriented particle chains are shown in Figure 4.1.1.g.

But as the particles rotate they come closer to the sidewalls, which exerts a repulsive force on the particles, restricting their further movement. Now the interaction between the particles becomes too complicated because of the simultaneous repulsive and attractive forces acting.

This restriction to the movement of the particles fastens the process of chains merging together to form columns as can be observed from Figure 4.1.3.h and Figure 4.1.3.i. The columns formed are also parallel to the electric field direction. This stage, during which the chains migrate and form columns, progresses even more slowly as the electrostatic force between the chains is very weak. The hydrodynamic forces are also

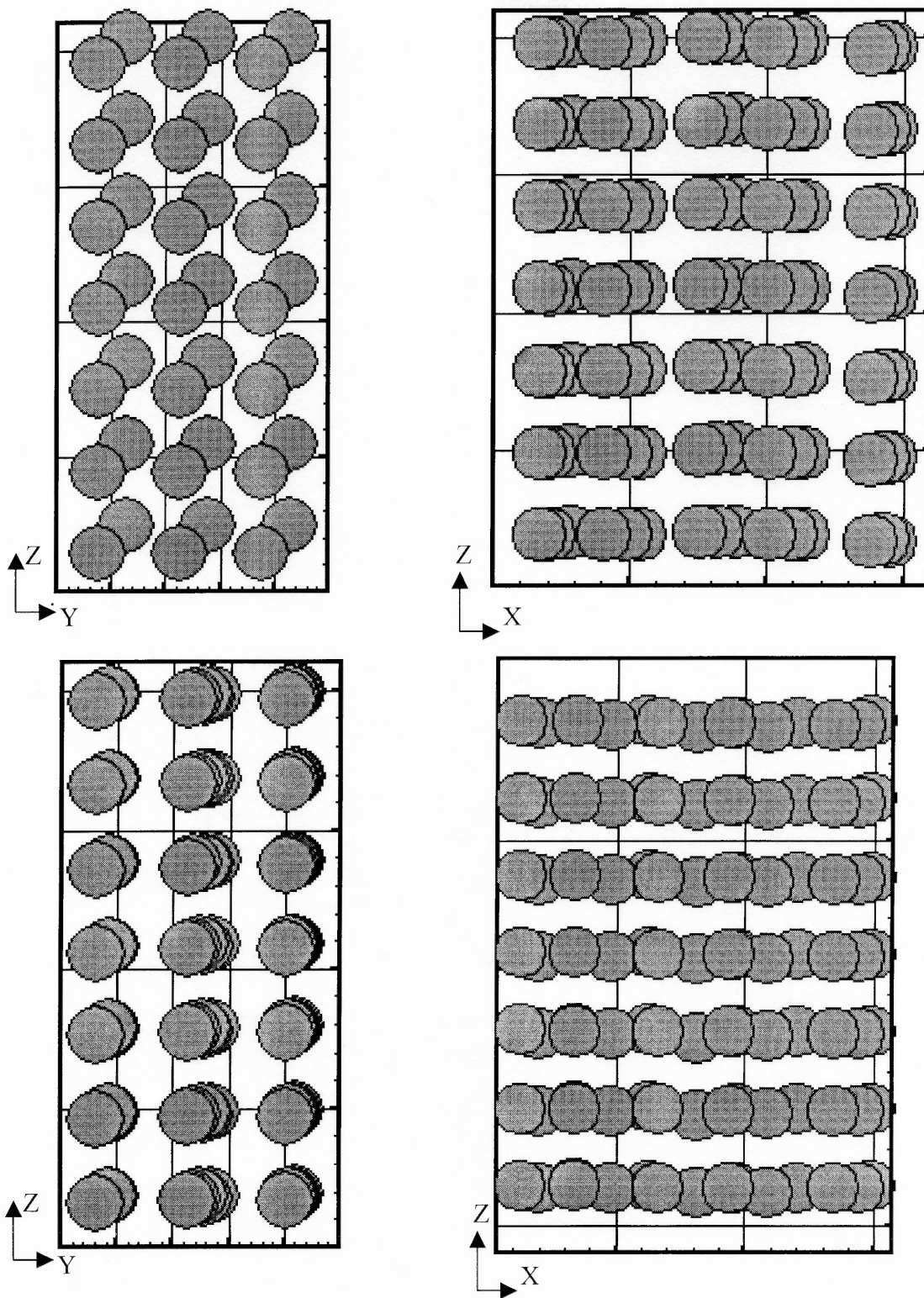


Figure 4.1.3 Particle positions at different times, a. $t = 0$ s, b. $t = 0.035$ s, c. $t = 0.08$ s, d. $t = 0.08$ s

important during this stage, as the drag force on a long rod-like chain is much larger than on a single particle. Another phenomenon noticed during the column formation is that the chains move away from the center, towards the $y = \text{constant}$ side walls, to form columns (Figure 4.1.3.j). This is probably an edge or boundary effect. In this simulations it is quite pronounced because the domain size is only five times larger than the particle diameter. Also notice that this migration of the chains towards the sidewalls does not occur along the z -direction because the domain is periodic along the z -direction. Finally, when the particles of the chains and columns rearrange such that the net force acting on all the particles vanish, a new state of equilibrium is established and the particle scale structure does not show any appreciable change.

The above results are similar to those obtained by Klingenberg, Swol and Zukoski [35]. They noted that the process of chain and column formation could be divided into three stages. In the first stage, small clusters or chains parallel to the direction of electric field are formed. In the second stage, which they termed the percolation threshold stage, the clusters grow, or the chains become thicker, and extend from one electrode to the other. In the third stage, the cluster distribution becomes periodic and at the end of this stage the particles stop moving. During the second and third stages, there is a dramatic increase in the viscosity of the ER suspension due to the formation of columns that extend between the electrodes which resist shearing. These numerical results are in qualitative agreement with the experimental observations of Wen, Zheng and Tu [59]. They have also noticed that the structure of ER suspensions evolves in three stages, as noted above.

On comparison with these above mentioned simulation studies it is easy to see

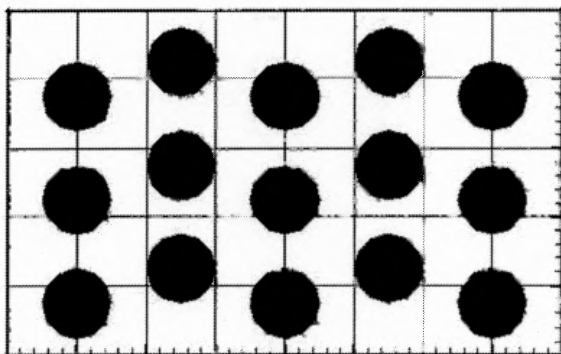


Figure 4.1.3.e Initial staggered position of the particles in the xy plane.

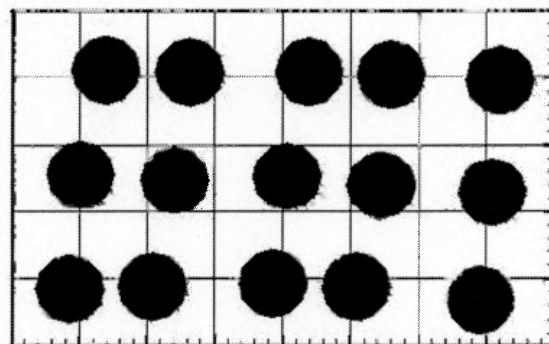


Figure 4.1.3.f Straight chains at time $t = 0.035\text{s}$ in the xy plane

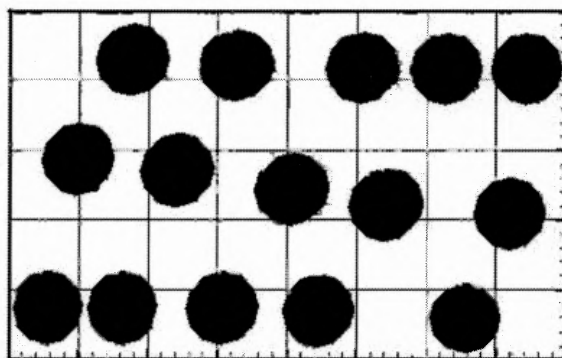


Figure 4.1.3.g Oriented chains as seen from the xy plane at time $t = 0.2\text{ s}$

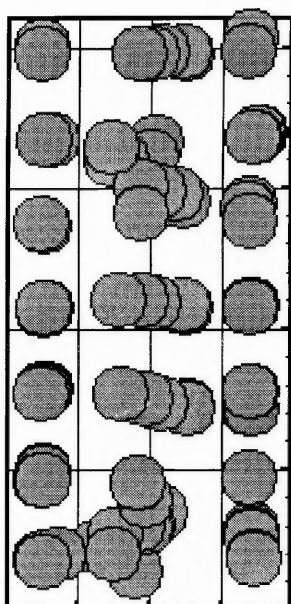


Figure 4.1.3.h
zy view of column formation

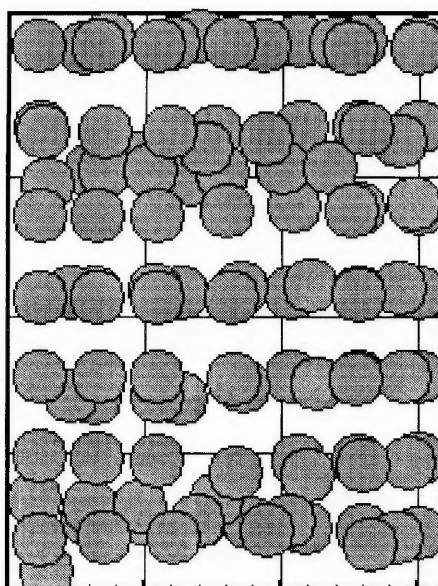


Figure 4.1.3.i
zx view of column formation

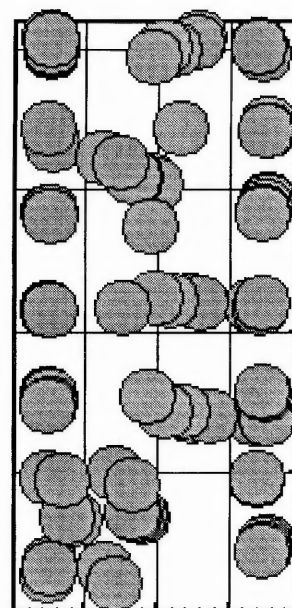


Figure 5.1.3.j
Columns moving to sidewalls

that the featured structure of ER suspensions has been obtained in our simulations using direct simulation method. Furthermore, the time required for the formation of the chain structures are found to be in agreement with observed experimental facts, which proves the advantage of using our simulation method.

4.1.4 Behavior of 105 Particles in a Channel Subjected to Pressure Driven Flow

In this section, the motion of 105 particles in a channel subjected to a pressure gradient of 20 in the z-direction is discussed. All other parameters, including the electric field strength, are the same as for the case described in the previous subsection.

For the pressure driven flows the chain formation process can be divided into three stages. In the first stage, which is similar to the first stage for the case where the pressure gradient is zero, neighboring particles rearrange such that the lines joining their centers become parallel to the electric field direction. During this stage, the hydrodynamic forces do not have appreciable influence on the particle motion, as their magnitude is small compared to that of the electrostatic forces. This results in the formation of regular chains as shown in Figure 4.1.4.a. The chains become better organized at $t = 0.08$ s.

At $t = \sim 0.08$ s the particle velocity due to the applied pressure gradient reaches close to the steady value and the magnitude of the hydrodynamic forces becomes comparable to the electrostatic forces. As discussed before in section 4.1.2, the hydrodynamic force tends to bend the chains formed during the first stage. Hence after time $t = 0.08$ s the particles at the center of the domain move faster than those near the

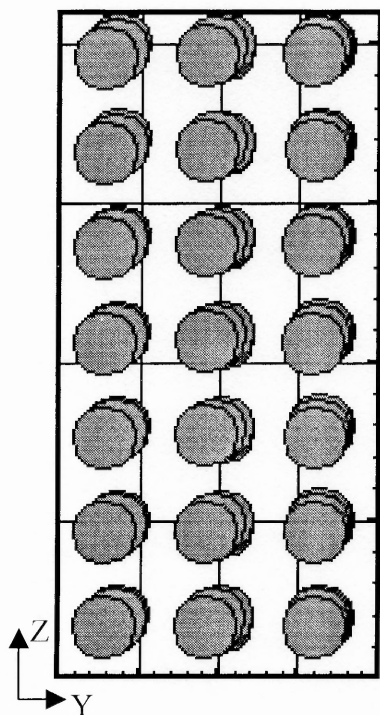


Figure 4.1.4.a Straight chains formed at $t = 0.08s$

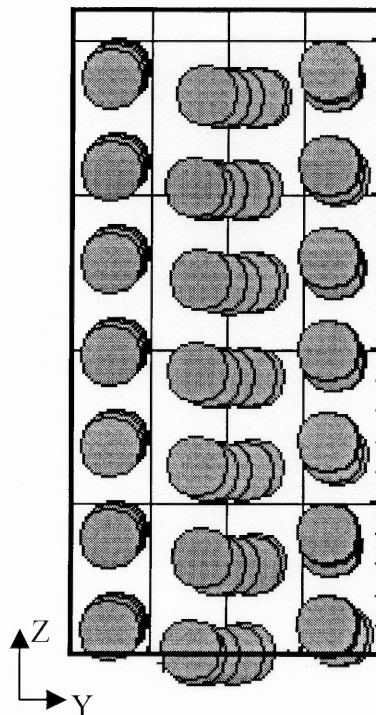


Figure 4.1.4.b Parabolic chains

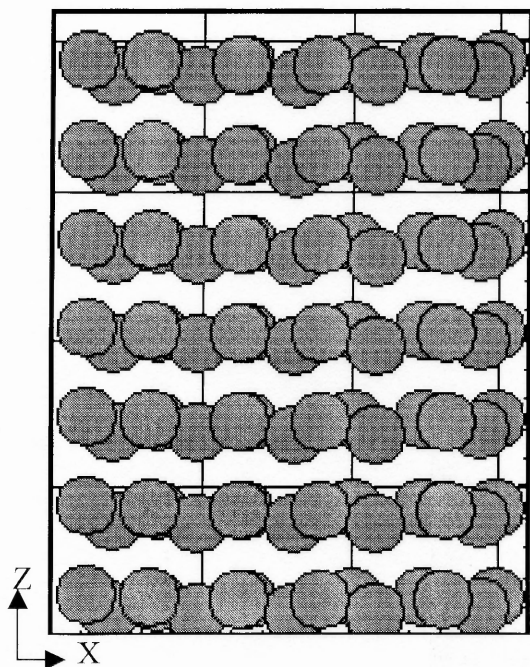


Figure 4.1.4.c Straight chains converted to parabolic ones at $t = 0.15 s$ due to the imposed flow

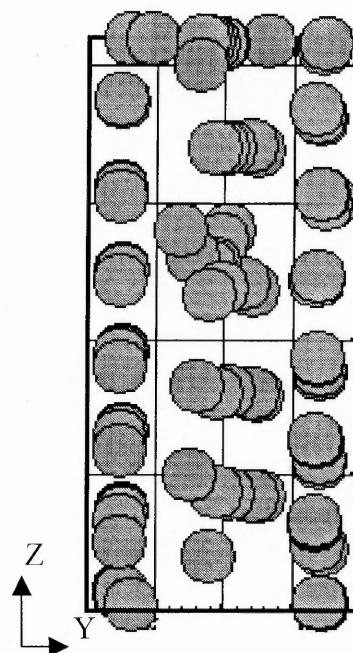


Figure 4.1.4.d Chains merging together to form columns.

domain sidewalls as the velocity profile is approximately parabolic. The particles are seen to align in a parabolic chain during this time period as can be observed from Figure 4.1.4.b and Figure 4.1.4.c. The degree of bending depends on the relative strengths of the hydrodynamic and electrostatic forces. This process continues till time $t = 0.15$ s.

Here also the particles are seen to rotate in the xy plane because of the torque developed and the rotation is restricted as the particles reach closer to the sidewalls.

With further increase in simulation time the particle chains begin to interact leading to merging of chains and formation of particle columns, parallel to the electric field direction (Fig. 4.1.4.d). This process of column formation is observed to begin at time $t = 0.15$ s. The process starts at a slow rate and then speeds up with time. This is because the electrostatic force of attraction between the particles is inversely proportional to the fourth power of the distance between the particles. Initially when the particles are in separate chains, the distance between them is more and therefore the electrostatic force of attraction is weak between them. As time progresses, the distance between the particles reduce, thus resulting in a rapid increase in the attractive forces, which in turn speeds up the process of rearrangement. Here also the particles from the chains at the center of the domain are seen to move to the chains at the sides of the domain to form columns. Once stable columns are formed, the structure of the ER solution does not show any appreciable change with time and the basic chain and column structures are preserved even though the particles continue migrating between the chains.

4.2 Non-uniform Electric Field

4.2.1 Convergence

To show that the results converge with mesh and time step refinements in the case of non-uniform electric field also, the transient motion of two particles subjected to the non-uniform electric field, as shown in Figures 4.2.1.a-b, is considered. The applied pressure gradient is assumed to be zero. Notice that even though the pressure gradient is zero, the fluid velocity and the electric field are assumed to be periodic in the z-direction, and the electrostatic particle-particle interaction force is computed by accounting for the periodicity.

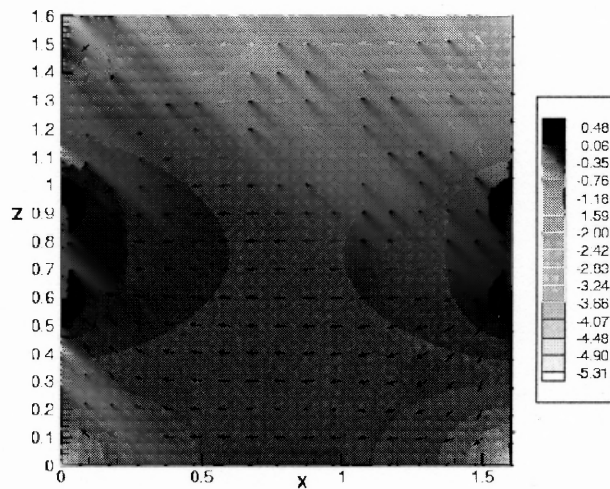


Figure 4.2.1.a Isovalues of $\log(|\mathbf{E}|)$ and the direction of \mathbf{E} on the domain midsection are shown. Notice that the electric field is maximum on the electrode tips. The electric field does not vary with y .

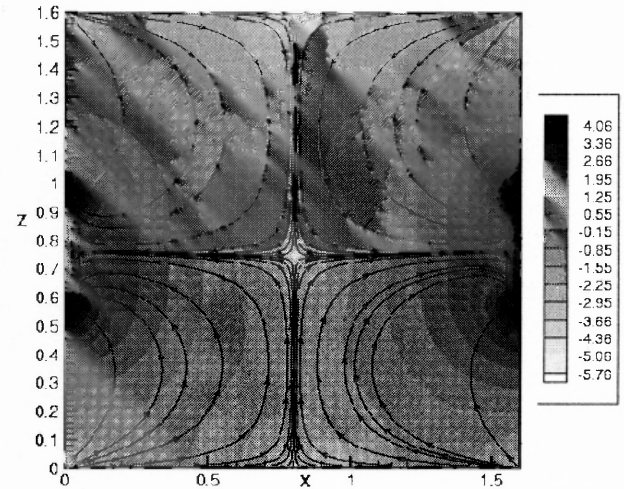


Figure 4.2.1.b Isovalues of $\log(|\mathbf{E} \cdot \nabla \mathbf{E}|)$ and the lines of dielectrophoretic force are shown. $\mathbf{E} \cdot \nabla \mathbf{E}$ does not vary with y .

The domain used in this study is 1.6 mm x 0.4 mm x 1.6 mm. At $t = 0$, two particles with $\beta = 0.297$ are placed at the initial positions (0.4 mm, 0.2 mm, 1.4 mm) and (1.2 mm, 0.2 mm, 1.4 mm) respectively, as shown in Figure 4.2.1.c. The electric field is generated by placing two 0.4 mm long electrodes in the domain walls parallel to the yz -coordinate plane, as shown in Figure 4.2.1.c. The left side electrode is grounded and the electric potential for the right side electrode is assumed to be 1.0. Isovalues of the electric field magnitude and the magnitude of $\mathbf{E} \cdot \nabla \mathbf{E}$ are shown in Figures 4.2.1.a-b. The values of dimensionless parameters are: $Re = 40.03$, $P_1 = 0.111$, $P_2 = 0.0992$ and $P_3 = 0.111$. The Mason number is 1.12, P_4 is 0.892 and P_5 is 1.0. As the parameters P_2 and P_3 are approximately equal, the electrostatic particle-particle interaction and dielectrophoretic forces acting on a particle are of the same order of magnitude.

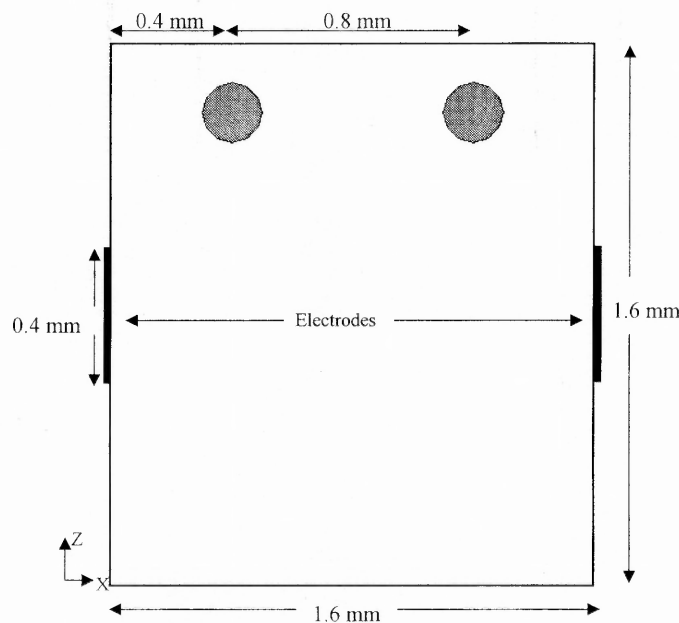


Figure 4.2.1.c The domain midsection normal to the y -axis is shown. The domain width along the y -direction is 0.4 mm. The cross-section is the same for all values of y . Also shown are the electrode locations and the initial positions of the two particles. The potential is prescribed on the electrode surfaces and the normal derivative of the potential is assumed to be zero on the rest of the boundary. The velocity is assumed to be periodic in the z -direction and zero on the other domain surfaces.

The initial positions of the two particles in this case were selected such that the magnitudes of the electrostatic particle-particle interaction force and the dielectrophoretic force are comparable. Thus, once the simulation is started, the particles move toward each other, and at the same time, each one moves towards the electrode closer to it due to the dielectrophoretic force. The particle on the left side moves towards the left electrode and the right side particle moves towards the right electrode. As the distance between the particles and the electrodes decreases, the dielectrophoretic force becomes greater than the electrostatic particle-particle interaction force. This causes the particles to move away from each other and toward the edges of the electrodes where they are collected approximately at $t = 0.5$ s.

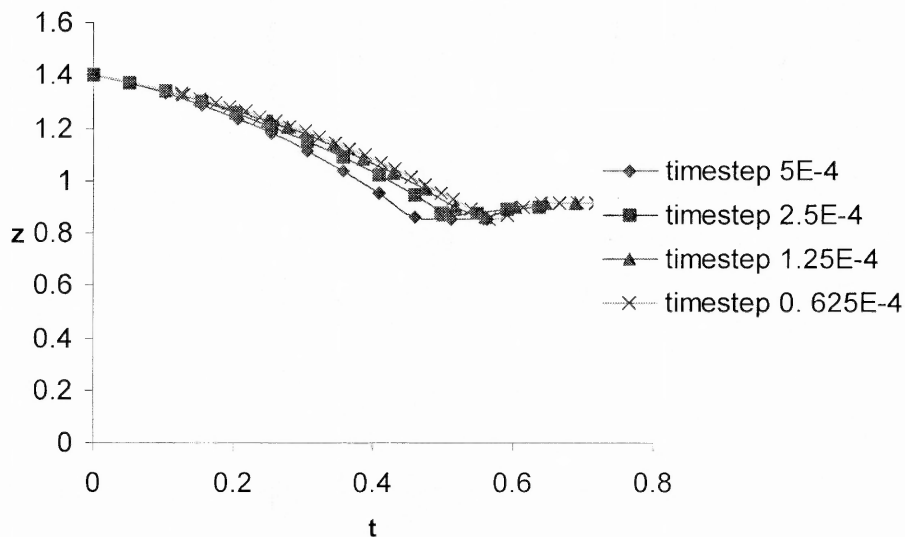


Figure 4.2.1.d The z -coordinate of the second particle is plotted as a function of time for four different values of the time step. The particle positions for the smallest two time steps are almost the same which proves that the numerical results converge with time step refinement.

To show that the results converge when the time step size is reduced, the z-coordinate of the second particle is plotted as a function of time for four different values of the time steps: 5×10^{-4} s, 2.5×10^{-4} s, 1.25×10^{-4} s and 0.625×10^{-4} s (see Figure 4.2.1.d). The number of velocity nodes for all four cases is 71,825. Since the trajectories for the smallest two time steps are approximately the same, it can be concluded that the results converge as the time step is reduced.

In order to show that the results also converge with mesh refinement, simulations were performed for three different mesh sizes. The number of velocity nodes for the three cases were 71,825, 137,781 and 549,153, respectively. The time step used for these calculations was 5×10^{-4} s. For the three mesh refinements, the z-coordinate of the second particle is plotted as a function of time in Figure 4.2.1.e. As the trajectories of the particles for the two finer meshes are approximately the same, it may be concluded that the results are also independent of mesh resolution.

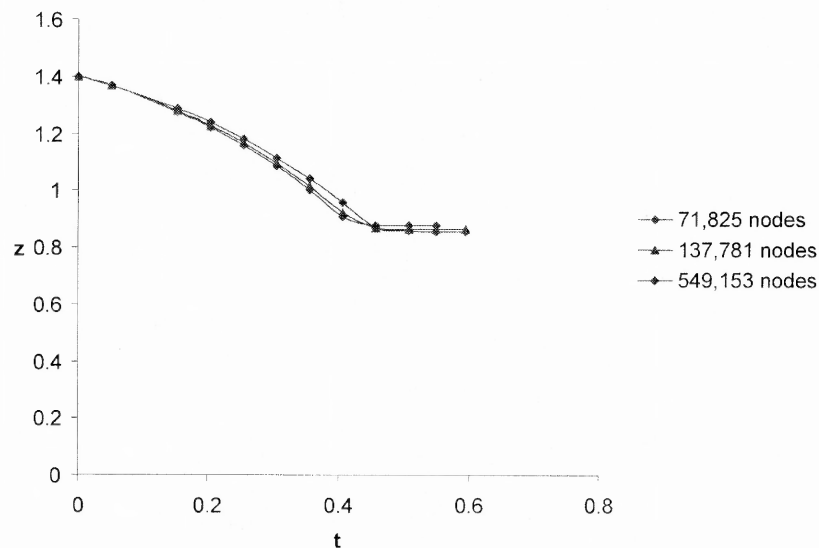


Figure 4.2.1.e The z-coordinate of the second particle plotted as a function of time for three different mesh sizes. The particle positions for the two finer meshes are virtually identical implying that the results converge with mesh refinement.

4.2.2 Cases With $dp/dz=0$

In this section, the transient motion of 40 particles in a channel subjected to a non-uniform electric field is studied. The pressure gradient in the z-direction for all cases in this subsection is assumed to be zero. The channel dimensions are 1.6 mm, 0.8 mm and 2.4 mm, in the x-, y- and z-directions. The non-uniform electric field is generated by placing two pairs of 0.6 mm long electrodes in the channel walls parallel to the yz-coordinate plane, as shown in Figure 4.2.2.a. The direction and magnitude of the electric field and $|\mathbf{E} \cdot \nabla \mathbf{E}|$ are shown in Figures 4.2.2.b-c.

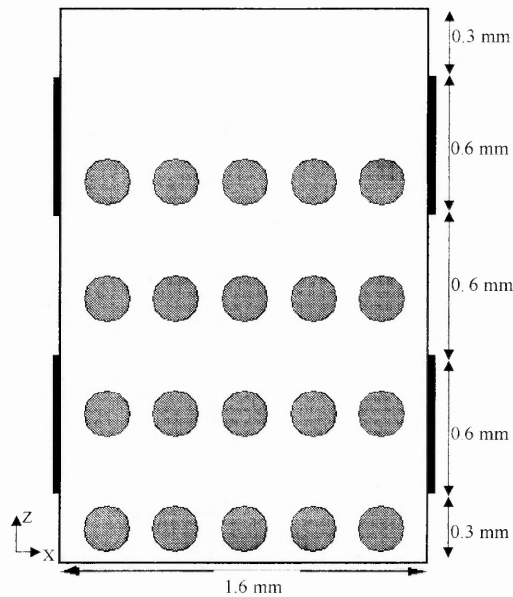


Figure 4.2.2.a The initial particle positions, on the midsection normal to the y-direction

For all results reported in this subsection, a uniform tetrahedral mesh with 208,065 nodes is used and the time step is 5×10^{-4} s. The initial particle and fluid velocities are assumed to be zero. The solids fraction is 0.0545. The values of the other parameters are $Re = 40.3$, $P_1 = 0.111$, $P_2 = 0.0993$, $P_3 = 0.111$, $Ma = 1.12$, $P_4 = 0.892$ and $P_5 = 1.0$. The parameter $P_5 = 1.0$ because the characteristic particle velocity used for estimating the

dimensionless parameters is obtained by balancing the viscous drag and dielectrophoretic force terms, as already stated.

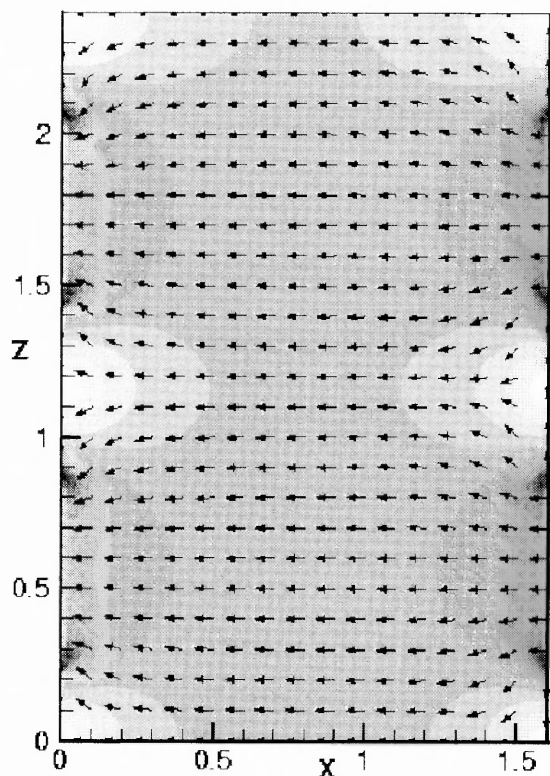


Figure 4.2.2.b Isovalues of the $\log(|\mathbf{E}|)$ on the domain midsection

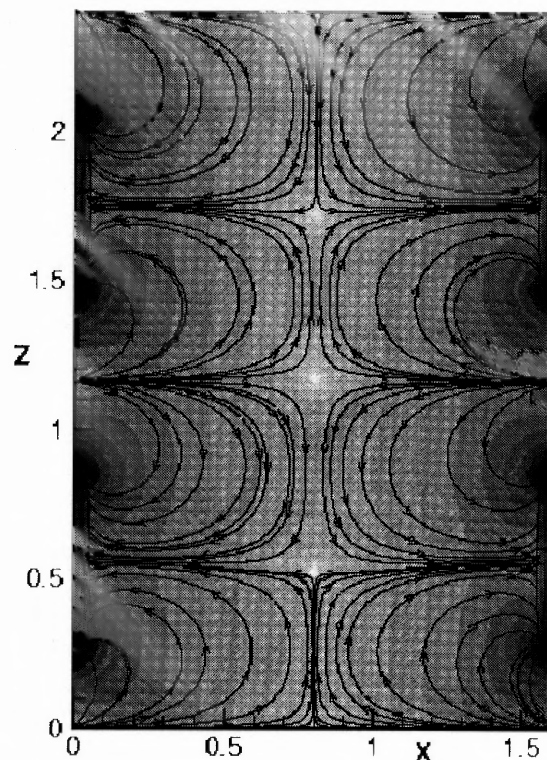


Figure 4.2.2.c Isovalues of $\log(|\mathbf{E} \cdot \nabla \mathbf{E}|)$ and lines of dielectrophoretic force

As explained earlier, in a non-uniform electric field, the particles are subjected to both the electrostatic particle-particle interaction and the dielectrophoretic forces, and thus their transient motion depends on the magnitudes and directions of both \mathbf{E} and $\mathbf{E} \cdot \nabla \mathbf{E}$. Figure 4.2.2.b shows that in the middle of the domain the electric field is relatively uniform and its direction is horizontal. The magnitude of $\mathbf{E} \cdot \nabla \mathbf{E}$, displayed in Figure 4.2.2.c, is relatively small near the domain mid plane on which it is zero at three inner points and the top. The bottom is the same as the top due to the periodic nature of the domain. Even though the dielectrophoretic force is zero at these points, the particles cannot accumulate there, since these points are the saddle points. This can also be seen in Figure 4.2.2.b,

which shows that the electric field is not locally minimum at these points. Assuming $\beta > 0$, the stable branch of the saddle point in the middle of the domain is horizontal and the unstable branch is vertical. For the two saddle points in between the electrodes the reverse is true, i.e., the stable branches are vertical and the unstable branches are horizontal. The lines of dielectrophoretic force shown in Figure 4.2.2.c indicate the direction of the force for $\beta > 0$.

The next two subsections describe the transient motion of the particles and their final positions for positive and negative dielectrophoresis, i.e., $\beta > 0$ and $\beta < 0$. As mentioned earlier, in the case where $\beta > 0$, the particles collect in the regions where the magnitude of the electric field is locally maximum, which is generally on the electrode surfaces, and for $\beta < 0$ they collect in the regions where the electric field is locally minimum.

POSITIVE DIELECTROPHORESIS: β POSITIVE

First, the case where $\beta = 0.297$, i.e., the dielectric constant of the particle is greater than that of the suspending fluid, is studied. Initially, the particles are arranged periodically as shown in Figure 4.2.2.a. There are four rows of particles in the z -direction, which do not cover the entire domain uniformly. The top row is close to the top pair of electrodes, and the third and fourth rows from the top are closer to the second pair of electrodes in the lower half of the domain. The second row from the top is exactly at the center of the domain and equidistant from the lower and upper electrode pairs. There are four layers of particles in the y -direction.

After the simulations are started, the top rows of particles move toward the upper electrode edges, and the third and fourth rows of particles from the top move toward the

lower electrode edges, since for these particles, the dielectrophoretic force is greater than the particle-particle interaction force. Also, notice that these rows of particles essentially break into three parts, with particles on the left moving toward the left electrodes, those on the right moving to the right electrodes and those near the middle staying in the middle (see Figure 4.2.2.d which shows particle positions at $t = 0.20$ s). For the second row of particles from the top since the dielectrophoretic force is small compared to the particle-particle interaction force, they first come close to each other and move toward the middle of the domain while maintaining their horizontal positions (see Figure 4.2.2.e).

It is interesting to notice that the particles in different rows along the y -direction initially do not interact with each other, but form separate chains. This is a consequence of the fact that there is no electric field variation in the y -direction and thus the dielectrophoretic force in the y -direction is zero. The particle-particle interaction force in the y -direction is not zero, but for $t < 0.20$ s it is small because of the symmetry of the initial particle positions.

As shown in Figure 4.2.2.e, at $t = 0.70$ s the particles that were initially near the domain midplane form chains. The orientation of these chains is determined by the stable and unstable directions of the saddle points of the dielectrophoretic force (see Figure 4.2.2.c). The chains are parallel to the stable direction of the saddle point and are formed because the particles under the action of the dielectrophoretic force move toward the zeros. Consequently, the chains near the center are horizontal and those near $z = 0.6$ mm and 1.8 mm are vertical. Once the chains are formed, the particles remain together in chains because of the electrostatic particle-particle interactions, but continue to move

towards the local maximum of the electric field under the influence of the dielectrophoretic force (Figure 4.2.2.f).

The chains near the domain mid plane experience a dielectrophoretic force that acts along the unstable branches of the saddle points and causes them to slowly move to the regions where the electric field magnitude is locally maximum, that is near the electrode tips. As more and more particles get collected, they start forming chains extending from the edges of the electrodes toward the center of the domain. The simulation was stopped at $t = \sim 13.3$ s, as all forty particles are nearly collected. The particle positions at this time are shown in Figure 4.2.2.g.

NEGATIVE DIELECTROPHORESIS: β NEGATIVE

In this subsection the simulation of particles with $\beta = -0.297$ is described. All other parameters, including the domain size and the initial particle arrangement, are the same as for the case of positive dielectrophoresis described in the previous subsection.

As expected, the motion of particles in this case, even at early times, is quite different from the case where β is positive. The particles do not move toward the electrode edges, where the electric field strength is locally maximum, but instead move toward the regions where the electric field strength is locally minimum. From Figure 4.2.2.b, it can be seen that the electric field strength is locally minimum on the domain walls in between the electrodes and at the top and bottom edges of the domain parallel to the xz -plane.

Once the simulations are started, the second row of particles located at the center of the domain move towards the sidewalls at the center and gets collected there around time $t = 0.2$ s (see Figure 4.2.2.h). This is due to the action of the dielectrophoretic force

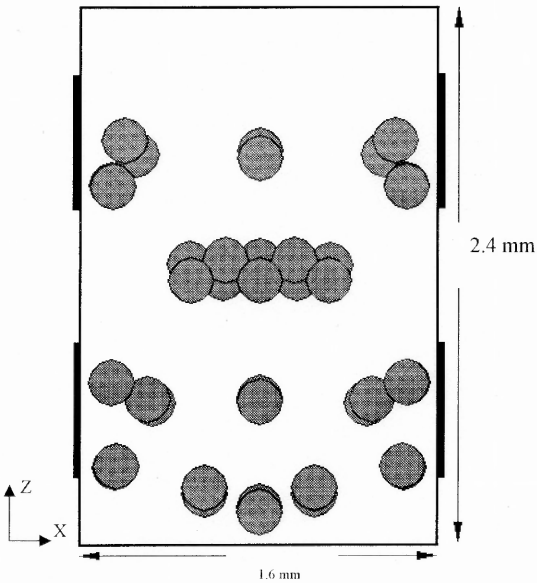


Figure 4.2.2.d The top view of the particle distribution at $t = 0.20$ s for $\beta = +0.297$.

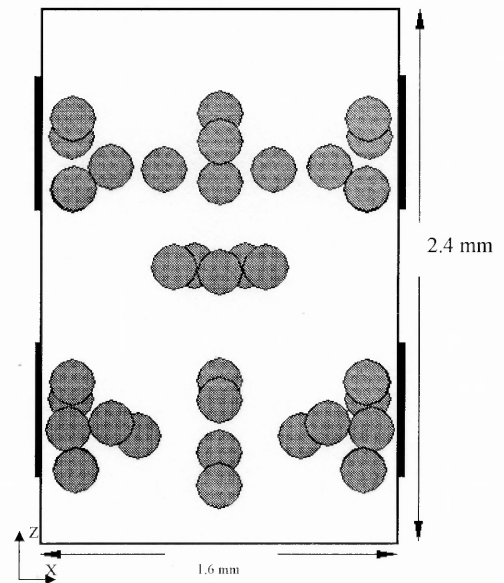


Figure 4.2.2.e The top view of the particle distribution at $t = 0.7$ s for $\beta = +0.297$.

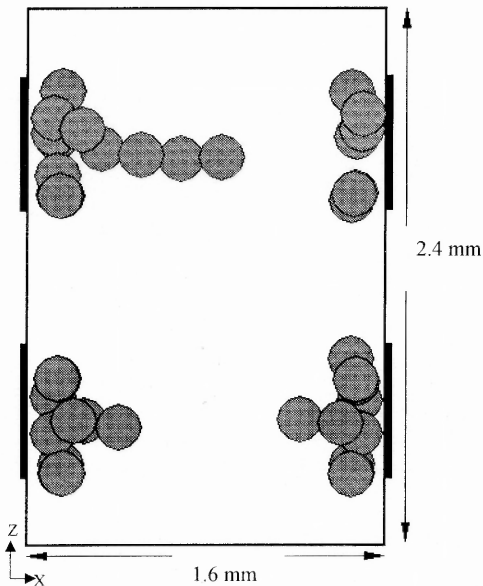


Figure 4.2.2.f The top view of the particle distribution at $t = 11.0$ s for $\beta = +0.297$.

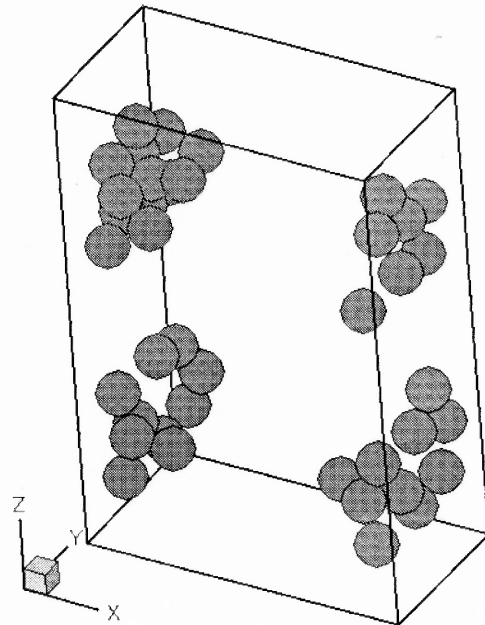


Figure 4.2.2.g An oblique view of the particle distribution at $t = 13.3$ s for $\beta = +0.297$.

which for $\beta < 0$ tends to move the particles away from the domain center along the horizontal branch of the saddle point at the center, which forms the unstable branch for the particles with negative β . The direction of the dielectrophoretic force for $\beta < 0$ is the opposite to that shown in Figure 4.2.2.c. Also recall that the directions of the stable and unstable branches of the dielectrophoretic force saddle points determine the orientation of the particle chains (see Figure 4.2.2.c). The chains near $z = 0.6$ mm and 1.8 mm are horizontal, in contrast to the case corresponding to $\beta > 0$ where the chains near these points were vertical.

The particles in the first, third and fourth rows from the top form inter-particle chains and move toward the regions where the electric field strength is locally minimum. Some of the chains move toward the top and bottom edges of the domain while the remaining migrate toward the center part of the domain, as can be seen in Figure 4.2.2.i. With further increase in time, all particles get collected in regions of low electric field strength at $t = 12.0$ s (see Figure 4.2.2.j).

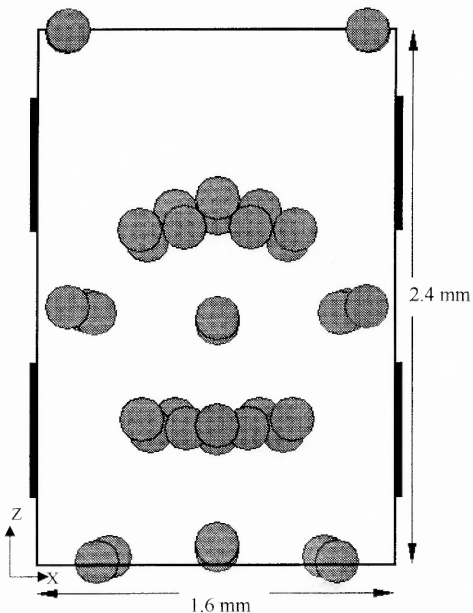


Figure 4.2.2.h The top view of the particle distribution at $t = 0.2$ s for $\beta = -0.297$.

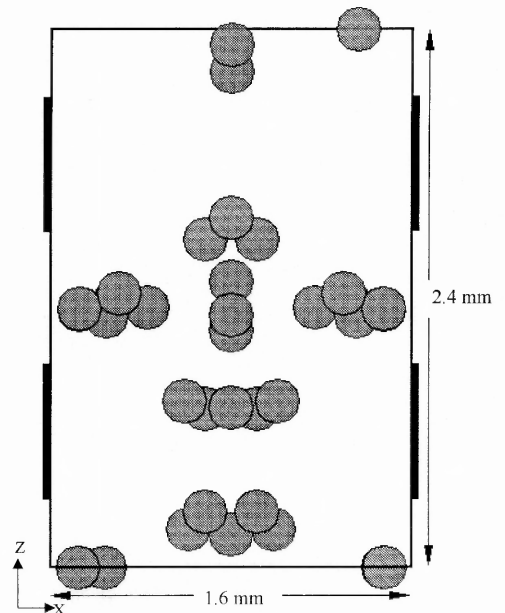


Figure 4.2.2.i The top view of the particle distribution at $t = 0.85$ s for $\beta = -0.297$.

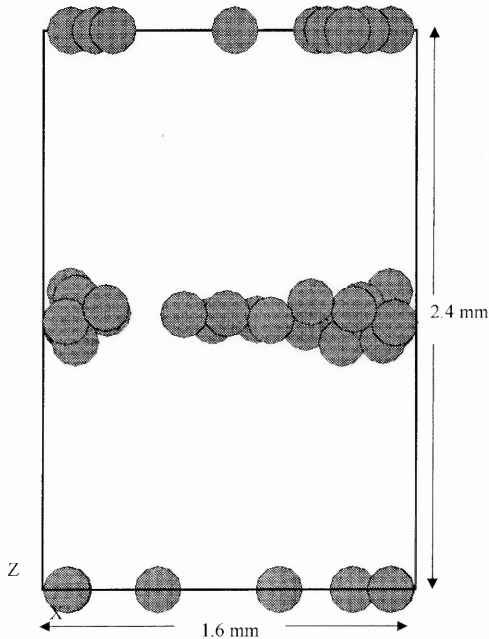


Figure 4.2.2.j The top view of particle distribution at $t \sim 12$ s for $\beta = -0.297$.

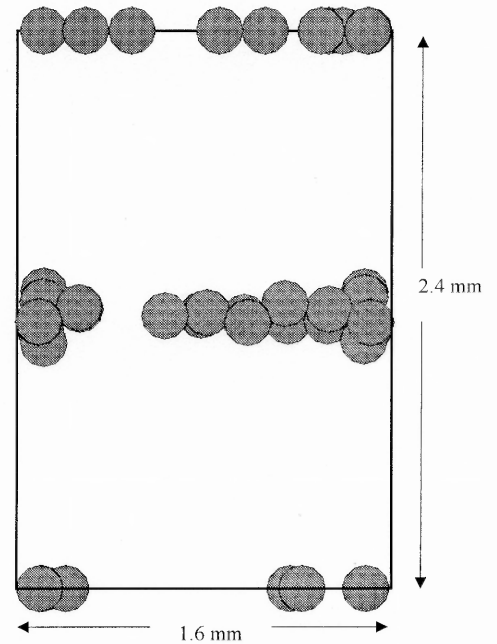


Figure 4.2.2.k The top view of particle distribution at $t = 16.4$ s.

As can be observed from Figure 4.2.2.j, the particle chains extend from the domain wall to the middle of the domain. The particle-particle interaction force is holding the particles together in chains. With further increase in simulation time, there is no noticeable change in the suspension microstructure (see Figure 4.2.2.k). The reason for this being, even though the particles are being pulled toward the region of low electric field, all of them cannot accumulate there because of space constraints.

COMPARISON WITH EXPERIMENTS

Extensive experimental studies were conducted in order to study the behavior of ER suspensions under non-uniform electric fields. Studies were conducted in both macro and

micro channels of various cross sections. One such experiment conducted for positive dielectrophoresis in a macro device is explained below.

The experimental device consisted of a 1.58 mm wide channel with electrodes located on the sidewalls of the channel as shown in Figure 4.2.2.1. Electrodes were made of a 1.58 mm square brass plates and were attached to the sides of the channel. Inlet and Outlet tubing connections were placed on the device to allow flow of fluid and particles through the channel. The flow rate was adjusted to be 2.08 ml/s. The maximum velocity of the fluid was 1.39 mm/s. The fluid and particles consisted of diesel fuel oil and hollow micro spheres. The density of the oil was 0.82 mg/mm^3 and its dynamic viscosity 2.0 mg/mm-s . The particles used were 0.75 mm diameter Extendspheres FM-1, hollow micro-spheres, PQ Corp. The particle density was 0.4 mg/mm^3 . The applied voltage was 2000V AC P/P amplitude at 300 hertz. The dielectric constant of the diesel oil at this frequency is about 1.75 and that of the Extendspheres is 3.0. The value of β for these values of dielectric constants is 0.192 and it is obvious from the sign of β that the particles will undergo positive dielectrophoresis and get collected at the edges of the electrodes where the electric field intensity is high. The values of other parameters calculated for the experiments are $Re = 0.021$, $P_1 = 429.65$, $P_2 = 655.84$, $P_3 = 429.65$, $Ma = 0.65$ and $P_4 = 1.53$. It can be observed from the value of P_4 that the experiments were conducted in a regime where both the particle-particle interactions and the dielectrophoretic forces are important and hence the particles will form particle chains while getting collected at the edges of the electrodes. The results obtained from one set of experiments are shown in Figure 4.2.2.1-o, which show that the particles collected are forming inter-particle chains.

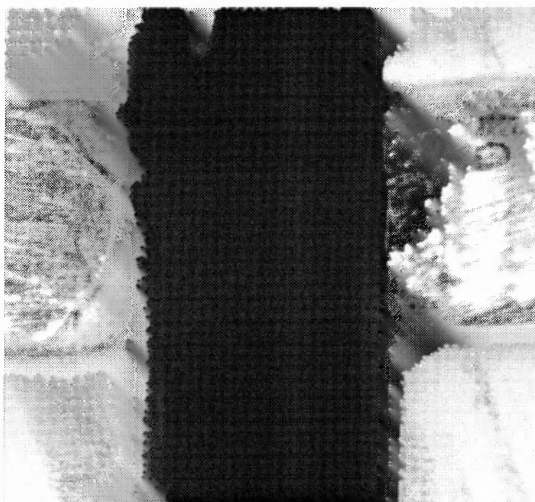


Figure 4.2.2.l A typical experimental setup showing the electrodes and the channel

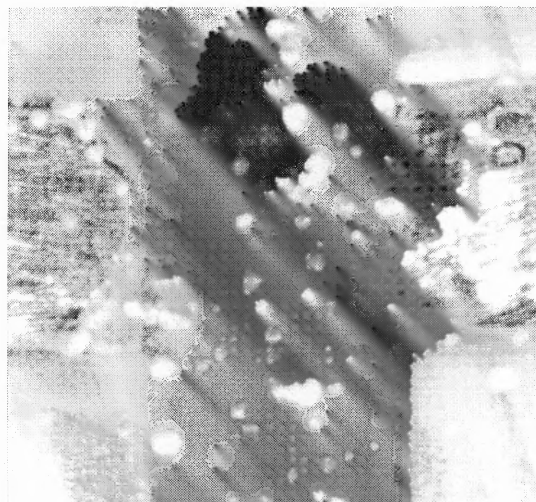


Figure 4.2.2.m ER fluid when initially introduced in the channel. The flow is from top to bottom.



Figure 4.2.2.n Particles collected at the edges of the electrodes in 1 minute.

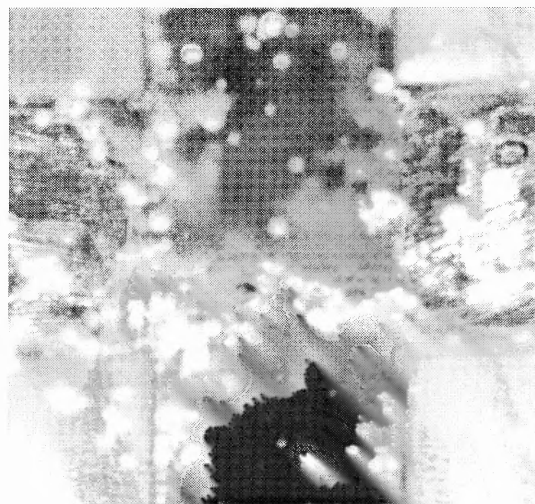


Figure 4.2.2.o Particles collected after 3 minutes. Notice the particles are extending as chains from the edges of the electrodes.

4.2.3 Cases with $dp/dz \neq 0$

In this section the case where a pressure gradient dp/dz is applied to the channel in the z -direction is considered. All other parameters are the same as in the previous section (4.2.2). The particles in this case are subjected to the hydrodynamic drag force, as well as the electrostatic dielectrophoretic and particle-particle interaction forces.

The particle distribution in pressure driven flows depends on the relative magnitudes of the hydrodynamic and electrostatic forces. Obviously, when the applied pressure gradient is very small, in the sense that the electrostatic forces dominate, the motion of particles is expected to be similar to that in section 4.2.2. On the other hand, if the applied pressure gradient is sufficiently large, in the sense that the hydrodynamic drag forces are much larger than the electrostatic forces, all particles will be swept away by the flow. In this work the regime in which the magnitudes of the electrostatic and hydrodynamic forces are comparable is investigated.

For sufficiently small particle concentrations, the velocity profile in a channel subjected to a pressure gradient is parabolic which implies that the particles near the channel center move faster than those near the channel walls. At higher particle concentrations, the parabolic velocity profile, as well as the dependence of the drag force on the distance from the channel center, is modified. The drag acting on a particle also depends on the particle concentration and their distribution within the channel, which, as already seen, is not uniform, especially when the electrostatic forces are strong.

First, the result for the case where the imposed pressure gradient is 1 dyne/cm^3 and $\beta = 0.297$ is presented. The pressure driven flow is along the negative z -direction. There are 40 particles, which are arranged periodically, as shown in Figure 4.2.2.a. As

discussed in section 2.3, based on the centerline velocity of the pressure driven flow, the dimensionless parameters Re , P_1 , P_2 , P_3 , Ma , P_4 and P_5 are 0.32, 13.9, 1550.0, 1740.0, 8.96×10^{-3} , 0.892 and 125.0, respectively. For all cases presented in this subsection, an alternative characteristic velocity can be computed by balancing the dielectrophoretic force and the viscous drag on the particles, as was done in the previous subsection. However, if this is done, then the dimensionless parameters will have the same values as in section 4.2.2. Also, notice that as P_2 and P_3 are approximately equal, the electrostatic particle-particle interaction and dielectrophoretic forces acting on a particle are of the same order of magnitude. Here, notice that the characteristic particle velocity obtained from the balance of viscous drag and dielectrophoretic force is approximately 10-100 times larger than that for the simulations. This is a consequence of the fact that the spatial distribution of $\mathbf{E} \cdot \nabla \mathbf{E}$ is non-uniform and that its magnitude in the domain middle, away from the electrodes, is smaller than that near the electrodes.

After the simulations are started, the pressure driven flow gains strength with time and the flow rate becomes steady at $t = \sim 0.45$ s. The hydrodynamic drag due to the flowing liquid moves the particles and particle chains in the downward direction, i.e., along the negative z -direction. Here again, the first, third and fourth rows of particles move toward the electrode edges whereas those in the second row form chains parallel to the x -direction. All particles, which are on the left and right sides of the domain, get collected near the electrode edges at $t \sim 0.45$ s (see Figure 4.2.3.a). For the case where the imposed pressure gradient is zero, the particle chains which are formed at the center of the domain, that is the chains formed by the second row of particles, remain parallel to the x -direction at all times and the particle chains near the center of the domain are

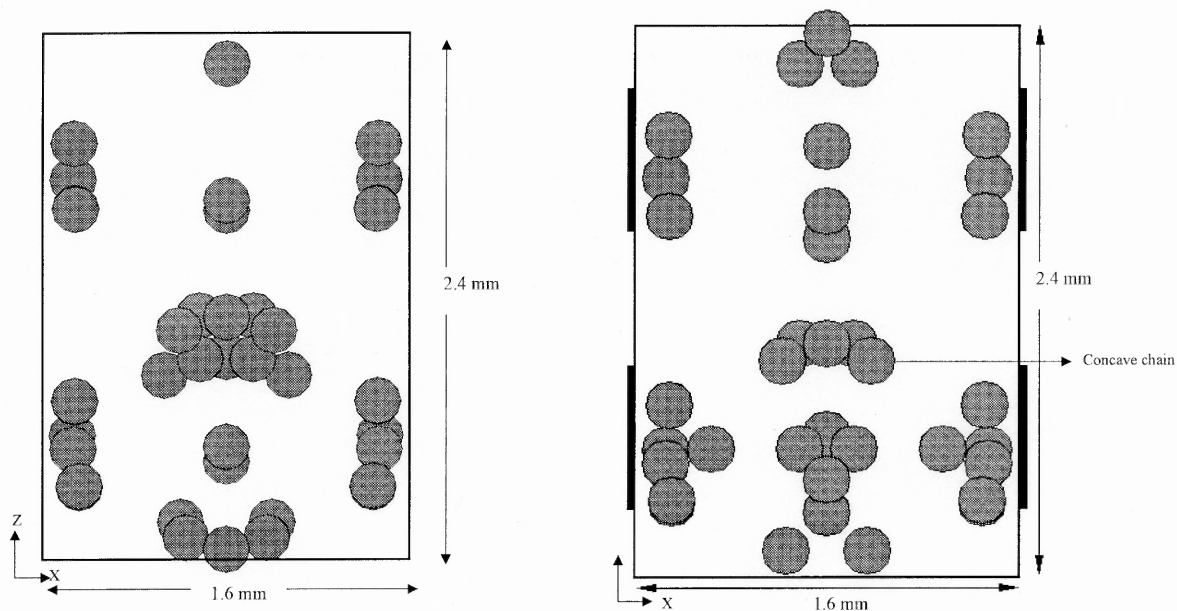


Figure 4.2.3.a The top view of the particle distribution at $t = 0.45$ s for $\beta = 0.297$ and pressure gradient $dp/dz = 1$ dyne/cm³. Notice that the particles collect near electrodes.

Figure 4.2.3.b $t = 0.8$ s for $\beta = 0.297$ and the pressure gradient $dp/dz = 1$ dyne/cm³. Notice the curved, concave down, chains near the center.

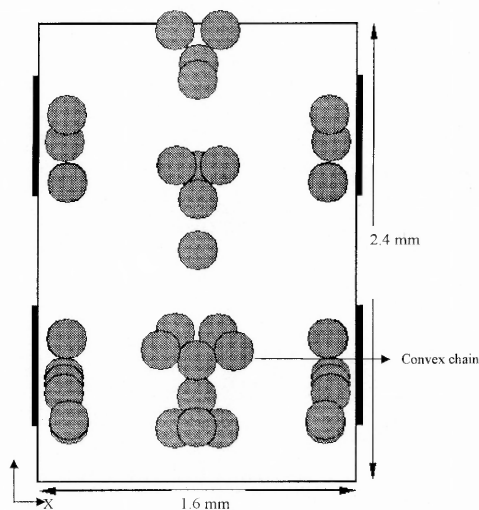


Figure 4.2.3.c $t = 1.5$ s for $\beta = 0.297$ and the pressure gradient $dp/dz = 1$ dyne/cm³. Notice the curved, convex up, chains.

pushed down by the pressure driven flow to the regions where they experience a larger downward dielectrophoretic force, especially those away from the domain midplane. This leads to the formation of the chains that are curved concave down, as shown in Fig. 5b. The chains continue to move downward with the flow and at $t \sim 0.8$ s some of the particles from the edges of the chains get separated and are collected on the lower pair of electrodes. At $t \sim 1.5$ s, the chains become convex up because of the parabolic flow, as can be seen in Figure 4.2.3.c.

The velocity of the particles and chains near the electrodes is smaller compared to those away from the electrodes because the fluid velocity near the walls is smaller and the electrostatic forces are stronger near the walls. In fact, the particles and chains close to the electrodes at times even move in the opposite direction of the flow. Most particles are collected near the electrode edges before $t \sim 9.0$ s. Notice that the particle collection time, in this case, is smaller than for the corresponding case with $dp/dz = 0$. This, as noticed above, is a result of the fact that the flow assists in the collection of particles by pushing them out of the regions where the dielectrophoretic forces are small.

Next, result for the case where the pressure gradient is increased to 2 dynes/cm^3 is presented. All other parameters are kept fixed. The magnitudes of the parameters Re , P_1 , P_2 , P_3 , Ma , P_4 and P_5 in this case are 0.64, 6.96, 388.0, 435.0, 0.0179, 0.892 and 62.6, respectively. Simulations show that the particles are collected in 8.0 s, which is smaller than for the case where the pressure gradient is 1 dyne/cm^3 .

Next, result for the case where the applied pressure gradient is 5 dynes/cm^3 is discussed. Eighty particles, for which $\beta = 0.297$, are present in the suspension and are initially arranged in a periodic manner, as shown in Figure 4.2.2.a. All other parameters

are the same as before and they are $Re = 1.6$, $P_1 = 2.78$, $P_2 = 62.0$, $P_3 = 69.7$, $Ma = 0.0448$, $P_4 = 0.892$ and $P_5 = 25.0$. The solids fraction is 0.118.

From Figure 4.2.2.c, it can be seen that $\mathbf{E} \cdot \nabla \mathbf{E}$ is periodic and that there are regions near the electrodes where the dielectrophoretic force moves the particles away from the electrodes and in the other regions the force moves the particles toward the electrodes. A particle moving along a streamline, therefore, experiences a dielectrophoretic force which, in some regions, tends to move it towards the electrodes and, in the other regions, away from the electrodes.

The initial fluid velocity due to the applied pressure gradient, in this case, is obviously larger and thus the particles that are initially pulled toward the electrodes cannot stick to the electrodes and, instead, keep moving in the downstream direction. After they enter the region where the dielectrophoretic force acts away from the electrodes, they indeed move away from the electrodes. Two such particles are shown in Figures 4.2.3.d-g. Since the electric field distribution is periodic, the escaped particles can be captured in the next period cell, at a later time, where the dielectrophoretic force acts towards the walls. This, however, increases the time needed for capturing all particles. Our simulations show that even if a particle is not captured, after every cycle its distance from the electrodes decreases, and thus the particle is eventually captured. This process for two particles, painted white, is described in Figure 4.2.3.d-g.

Also notice that the captured particles form chains that extend from the electrodes and are more obvious than in the case of zero pressure gradient $dp/dz = 0$ because the captured particles experience a hydrodynamic force that pushes them downwards while the dipole-dipole interaction force keeps them attached, leading to more apparent chains.

Next the case where the pressure gradient is 10 dynes/cm^3 is described. The parameters Re , P_1 , P_2 , P_3 , Ma , P_4 and P_5 are 3.2, 1.39, 15.5, 17.4, 0.0896, 0.892 and 12.5

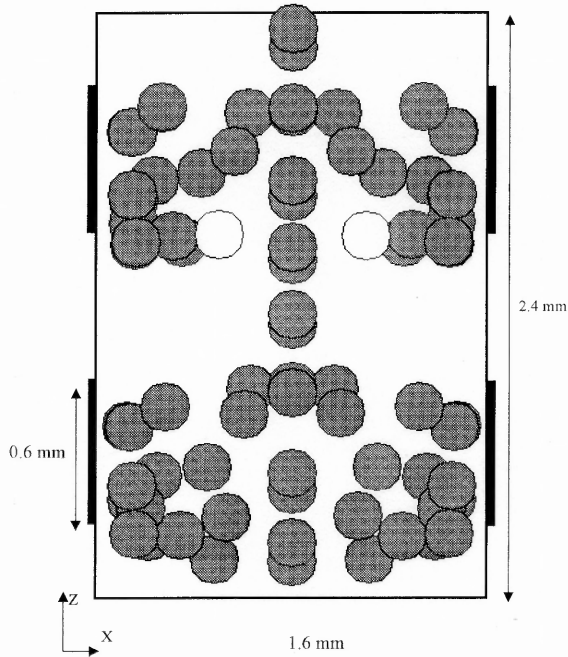


Figure 4.2.3.d The top view of the particle distribution at $t = 0.5 \text{ s}$ for the pressure gradient $dp/dz = 5 \text{ dynes/cm}^3$ and $\beta = 0.297$.

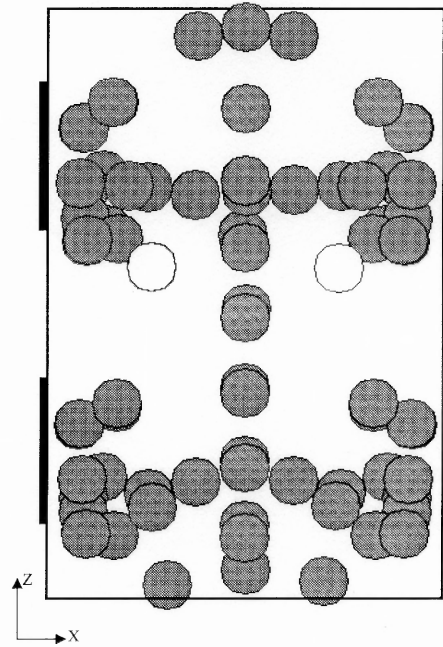


Figure 4.2.3.e $t = 1.0 \text{ s}$. The white particles, even though close to the electrodes, are being pushed downstream by the flow.

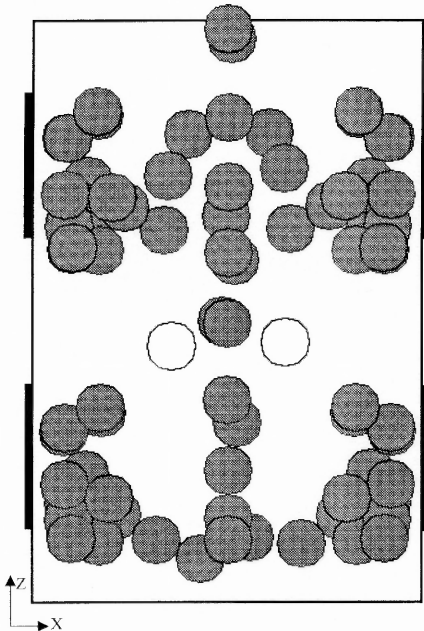


Figure 4.2.3.f $t = 1.40 \text{ s}$. The white particles are moving away from the electrodes, while getting closer to each other

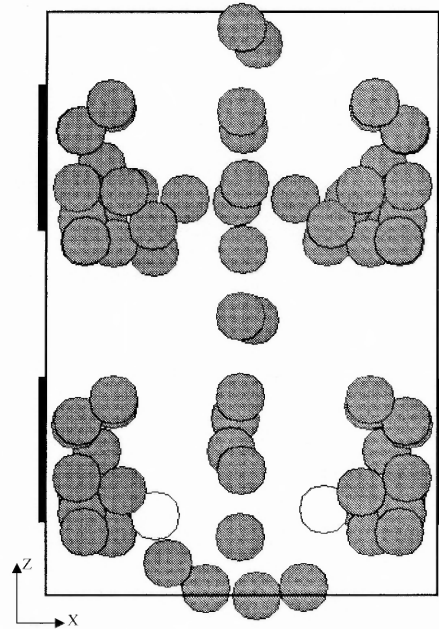


Figure 4.2.3.g $t = 2.0 \text{ s}$. The white particles are now captured by the lower electrodes.

respectively. The remaining parameters are the same as for the previous case. Since the hydrodynamic force in this case is stronger than previously discussed cases, the effect of the electrostatic force is felt only on the particles that are close to the electrodes. In particular, simulations show that the particles close to the electrodes decelerate when they are in the regions where the dielectrophoretic force acts against the flow direction. The dielectrophoretic force, however, is not strong enough to overcome the hydrodynamic drag and capture all the particles. The particles that are farther away from the electrodes move approximately along the undisturbed streamlines of the pressure driven flow.

4.2.4 Mixture Containing Particles with Positive and Negative β

It has been suggested in the past that the dielectrophoretic effect can be used to separate particles with different dielectric constants [20, 32]. To numerically study this phenomenon, we consider an electrorheological mixture containing two types of particles for which β values are different. For simplicity, we assume that for one set of particles $\beta = 0.297$ and for the second set $\beta = -0.297$. The imposed pressure gradient is assumed to be zero. The channel dimensions are 1.6 mm, 0.8 mm and 2.4 mm, in the x-, y- and z- directions. The non-uniform electric field is generated by placing two pairs of 0.6 mm long electrodes in the channel walls parallel to the yz-coordinate plane. The electrodes in the left are grounded, whereas the right electrodes are at a potential of 1 V. The direction and magnitude of the electric field and $|\mathbf{E} \cdot \nabla \mathbf{E}|$ are shown in Figures 4.2.2.b-c. For all results reported in this subsection, a uniform tetrahedral mesh with 208,065 nodes is used and the time step is 5×10^{-4} s. The initial particle and fluid velocities are assumed to be zero. Initially, 40 particles, 20 of each type, are periodically arranged in the domain as

shown in Figure 4.2.4.a. The particles with positive β are at the top and bottom layer in the y - direction, and the particles with negative β occupy the two middle layers. The values of the other parameters are $Re = 40.3$, $P_1 = 0.111$, $P_2 = 0.0993$, $P_3 = 0.111$, $Ma = 1.12$, $P_4 = 0.892$ and $P_5 = 1.0$. We remind the reader that the parameter $P_5 = 1.0$ because the characteristic particle velocity used for estimating the dimensionless parameters is obtained by balancing of the viscous drag and dielectrophoretic force terms.

In practice, for this technique to work, one must find a suitable liquid such that its dielectric constant is smaller than the dielectric constant of one set of particles and greater than the dielectric constant of the second set of particles. Since the frequency dependence of the dielectric constant is different for different materials, this can also be achieved by selecting a suitable frequency in certain cases [20].

Simulations show that, as expected, the particles with positive β move in the direction of $\mathbf{E} \cdot \nabla \mathbf{E}$ shown in Fig. 4.2.2.c and get collected in the regions of high electric field strength. The particles with negative β , on the other hand, move in the opposite direction of $\mathbf{E} \cdot \nabla \mathbf{E}$ and get collected in the regions of low electric field strength. It follows that the particles with different dielectric constants can indeed undergo separation.

The particles with negative β in the second row, i.e., those particles that are in the middle of the domain, move relatively quickly to the domain sidewalls at $z = 1.2$ mm and get collected there, as the horizontal branch of the saddle point in the middle of the domain is the unstable branch for $\beta < 0$. The particles in the second row for which β is positive move toward the position ($x = 0.8$ mm, $z = 1.2$ mm) and form horizontal chains

(as can be seen in Figures. 4.2.4.b-c), as the horizontal branch of the saddle point is the stable branch for $\beta > 0$. All positive β particles are collected at the tip of the electrodes.

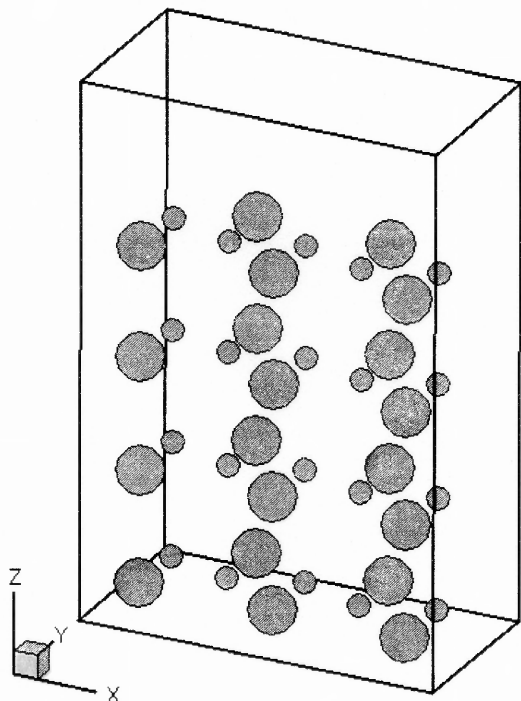


Figure 4.2.4.a An oblique view of the initial position of particles with $\beta < 0$ and $\beta > 0$.

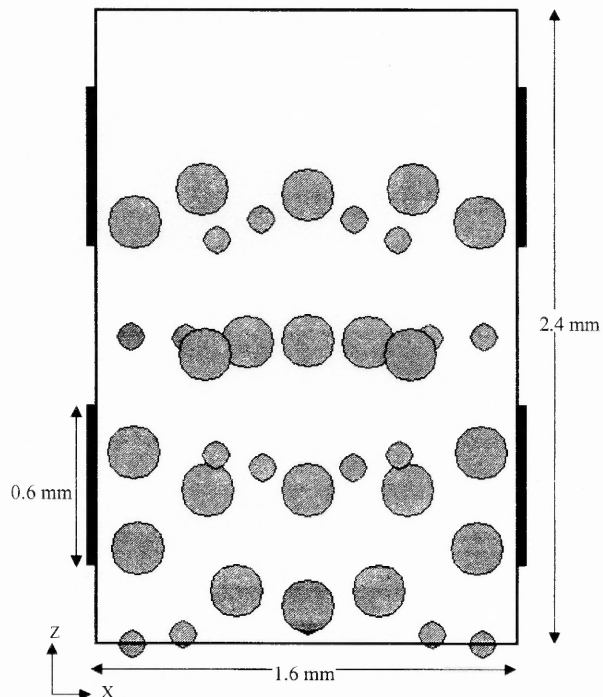


Figure 4.2.4.b The top view of particle distribution at $t = 0.3$ s.

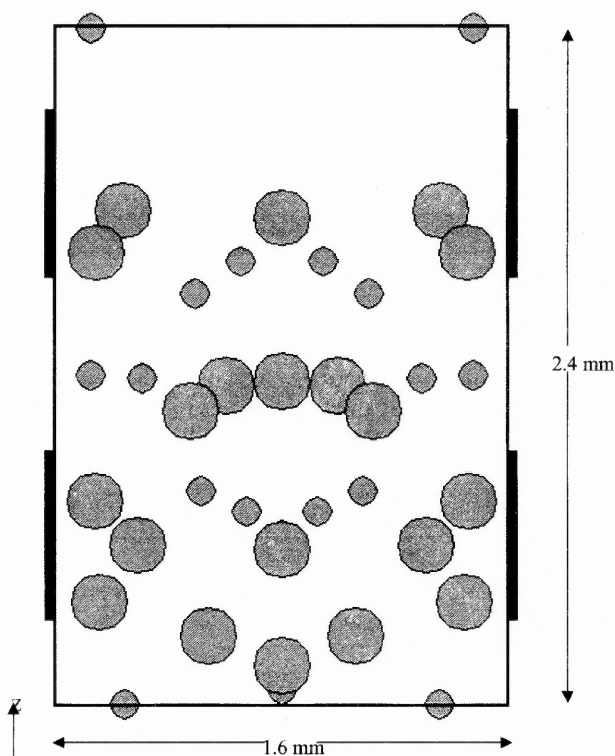


Figure 4.2.4.c $t = 0.5$ s

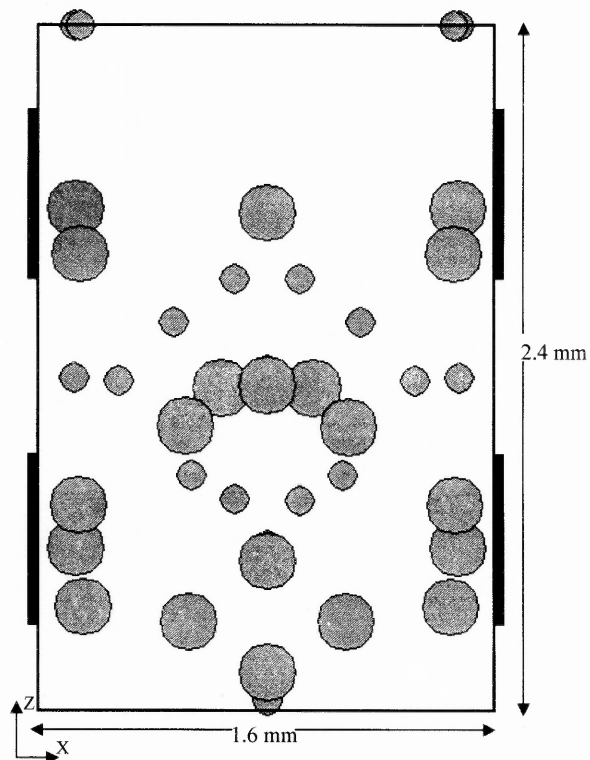


Figure 4.2.4.d $t = 0.8$ s

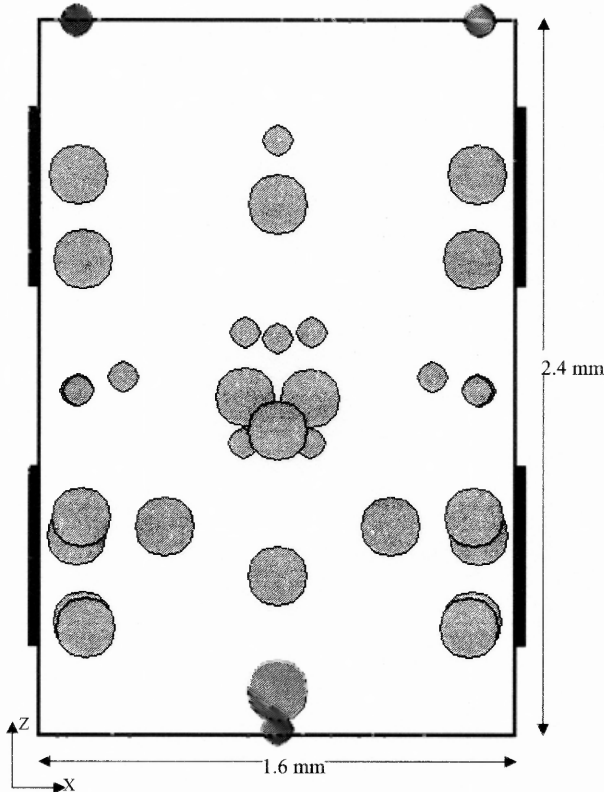


Figure 4.2.4.e $t = 2.5$ s

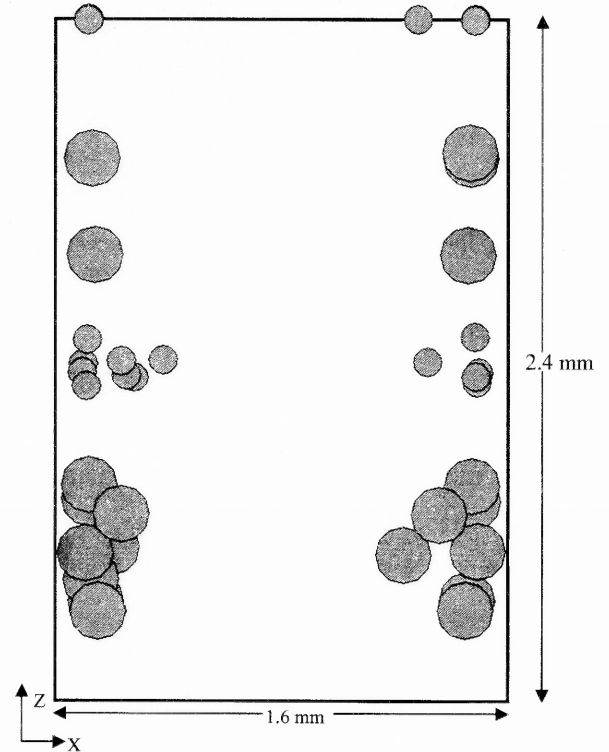


Figure 4.2.4.f $t \sim 14$ s

Moreover, the top three rows of particles for which β is negative get collected on the domain sidewalls at $z = 1.2$ mm and the fourth row gets collected at the position $z = 0$. All the particles in the domain get collected in about 14.0 s. The entire sequence of separation of particles, structure formation and eventual collection can be observed in Figures 4.2.4.a-f.

Next simulations are done for the same mixture of particles, but with the potential boundary conditions changed. This time the lower electrode on the left and the upper electrode on the right are grounded, whereas the other two electrodes are still maintained at a potential of 1 V. The distribution of electric field and the gradient of electric field are shown in Figures 4.2.4.g-h. This change in the potential boundary conditions results in

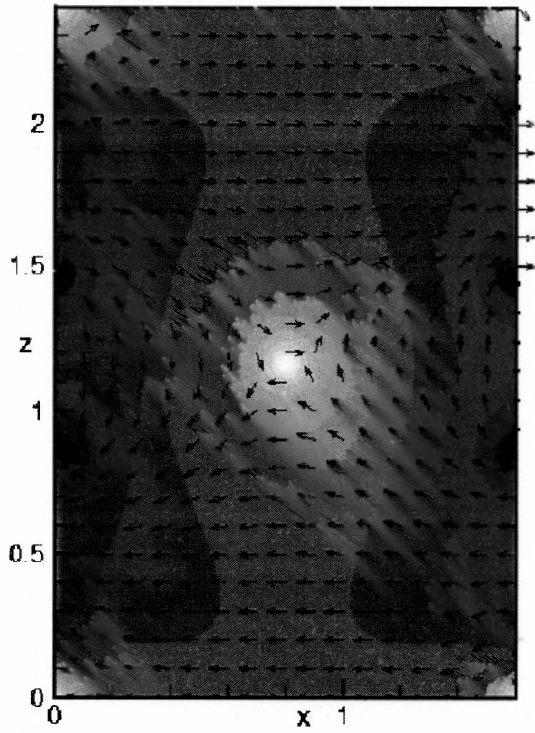


Figure 4.2.4.g Isovalues of $\log(|\mathbf{E}|)$ and the direction of \mathbf{E} on the domain midsection are shown.

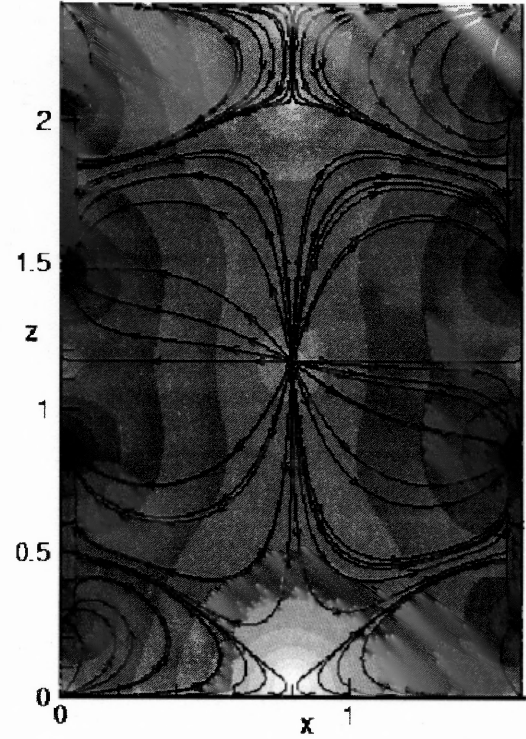


Figure 4.2.4.h Isovalues of $\log(|\mathbf{E} \cdot \nabla \mathbf{E}|)$ and the lines of dielectrophoretic force.

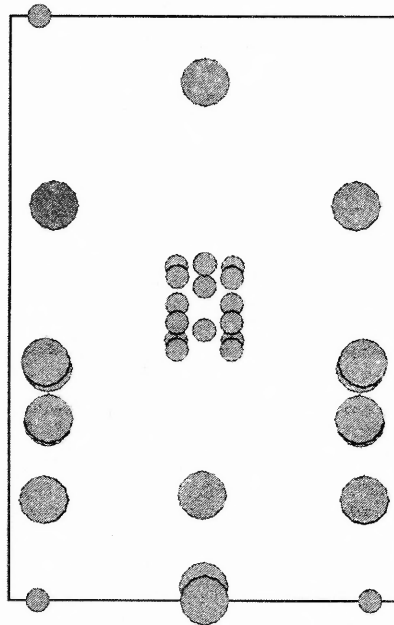


Figure 4.2.4.i The final position of the particles collected at $t = 3$ s

moving the stable regions of the local minimums of the electric field, where the particles can collect, from the domain sidewalls to ($x = 0.8$ mm, $z = 1.2$ mm). On simulations, the particles with negative β move quickly to the region of minimum magnitude of electric field at ($x = 0.8$ mm, $z = 1.2$ mm), whereas the particles with positive β move to the electrode edges where the electric field is maximum. Some of the particles with negative β also get collected at the sidewalls at the bottom of the domain, since stable local minimums of the electric field exists there too

All the particles in the domain get collected in time, $t = 3.0$ s, the particle positions for which time is shown in Figure 4.2.4.i.

4.2.5 Influence of Electric Potential Boundary Condition

Clearly, the particle motion and the regions in which they ultimately collect can be modified by changing the electric potential of the electrodes. This, of course, can be achieved also by changing the electrode positions, but in applications it is much more difficult to move the electrodes, especially when a time dependent electric field is applied.

More specifically, it is shown that the location of the local minimum of the electric field strength can be moved anywhere in the domain by changing the electric potential boundary conditions.

First simulations are done for the same conditions as in the second case for the previous subsection, i.e., by interchanging the charged and the grounded electrodes. This time all the particles used are having the same β value of either 0.297 or -0.297 , so that they all will collect in the region of maximum or minimum value of the electric field. The

distributions of \mathbf{E} and $\mathbf{E} \cdot \nabla \mathbf{E}$ for this case are shown in Figures 4.2.4.g and h. The maximum of the electric field is still at the tips of the electrodes, but the minimums have shifted to $(x = 0.8 \text{ mm}, z = 1.2 \text{ mm})$, i.e., the center of the domain and to the four corners of the domain. The locations of the saddle points of $\mathbf{E} \cdot \nabla \mathbf{E}$, i.e., where $\mathbf{E} \cdot \nabla \mathbf{E}$ is zero but $|\mathbf{E}|$ is not locally minimum or maximum, are also changed to $(x = 0.8 \text{ mm}, z = 0 \text{ mm})$ and $(x = 0.8 \text{ mm}, z = 2.1 \text{ mm})$.

The remaining parameters and the number of particles are the same as in the previous subsection. As before, for $\beta > 0$ the particles accumulate near the tips of the electrodes and for $\beta < 0$ they accumulate near the local minimums which are now located at different positions. The transient particle motion is also quite different from the case described in the previous subsection for positive β . Recall from the previous subsection for the case with positive and negative β particles mixed together, the particles with positive β in the second row came together as horizontal chains at the center of the domain (see Figures 4.2.2.d-e). However, in this case, the second row of particles in the middle of the domain move immediately to the sidewalls, instead of forming horizontal chains. In the previous subsection, the particle chains were formed because $\mathbf{E} \cdot \nabla \mathbf{E}$ contains a saddle point in the middle of the domain. However, in the present case there is a local minimum of $|\mathbf{E}|$ which causes the dielectrophoretic force to move the particles away from the center of the domain. In addition, the particles tend to move relatively quickly toward the electrode edges, since no chains are formed. Most particles are collected by the electrodes in approximately 2.55 s. The time taken for collection in this case is much smaller than for the previous case with the mixture of particles, even though

all parameters other than the sign of β are the same. This is due to the fact that, in this case, there are no saddle points for $\mathbf{E} \cdot \nabla \mathbf{E}$ in the middle of the domain.

The motion of particles with $\beta < 0$ is also qualitatively different from before. The particles collect at $(x = 0.8 \text{ mm}, z = 1.2 \text{ mm})$, as it is a stable region for $\beta < 0$ (Figure. 4.2.4.g-h). The other important difference is that the time required for all particles to collect in this case is about four times smaller than for the electrode configuration of the previous subsection. The final positions of the particles collected are shown in Figure.

4.2.5.a.

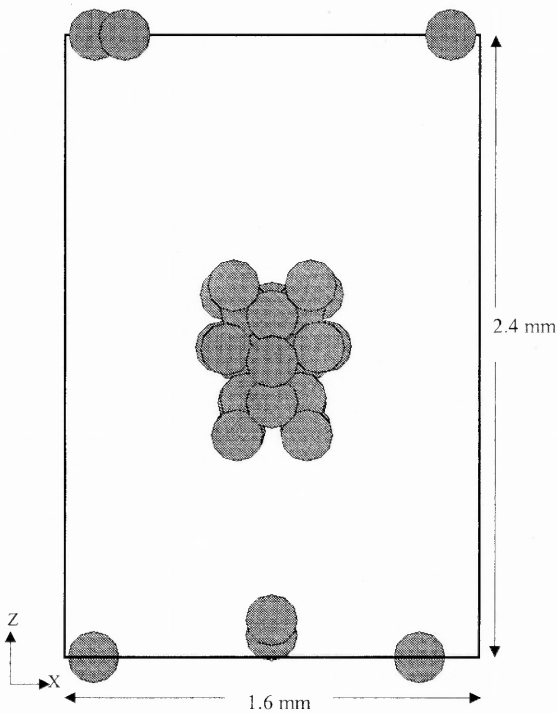


Figure 4.2.5.a The top view of the particle distribution at $t = 3 \text{ s}$ for $\beta < 0$.

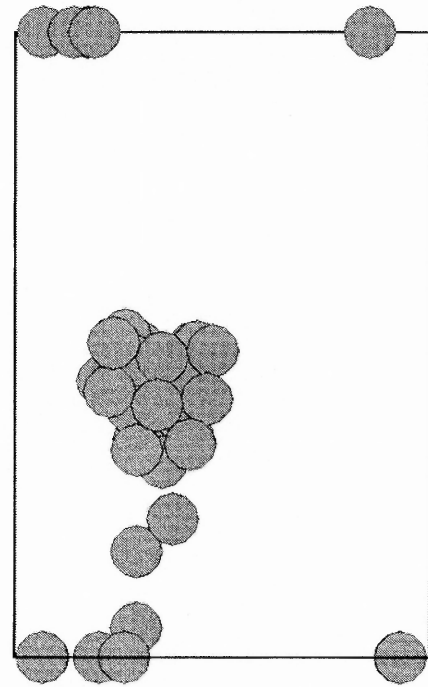


Figure 4.2.5.b The final position of the particles collected.

Next the minimum of the electric field at $(x = 0.8 \text{ mm}, z = 1.2 \text{ mm})$ is shifted to the left of the domain to $(x = 0.5 \text{ mm}, z = 1.1 \text{ mm})$, by changing the potential of the electrodes. For achieving this effect the bottom left electrode is kept at 0.5 V , the top left electrode is maintained at 0.2 V , the bottom right electrode is grounded and the top right

electrode is maintained at a potential of 1 V. On simulations using particles with negative β , they are seen to collect in the new local minimum region of the electric field at $(x = 0.5$ mm, $z = 1.1$ mm), and they are collected in around the same time as in the previous case. The final positions of the particles are shown in Figure. 4.2.5.b. For simulations with positive β particles, the particles are still collected at the electrode edges, since there is no change in the maximum regions of the electric field.

Further the minimum of the electric field is lowered to $(x = 0.8$ mm, $z = 0.8$ mm), by changing the potential of the bottom left electrode to 1 V, the top left electrode to the grounded state, and both the right electrodes to 0.5 V. As per expectations for simulations with negative β particles, the particles get collected in the new region of minimum magnitude of electric field. The final positions of the particles at time, $t = 0.9$ s is shown in Figure. 4.2.5.c.

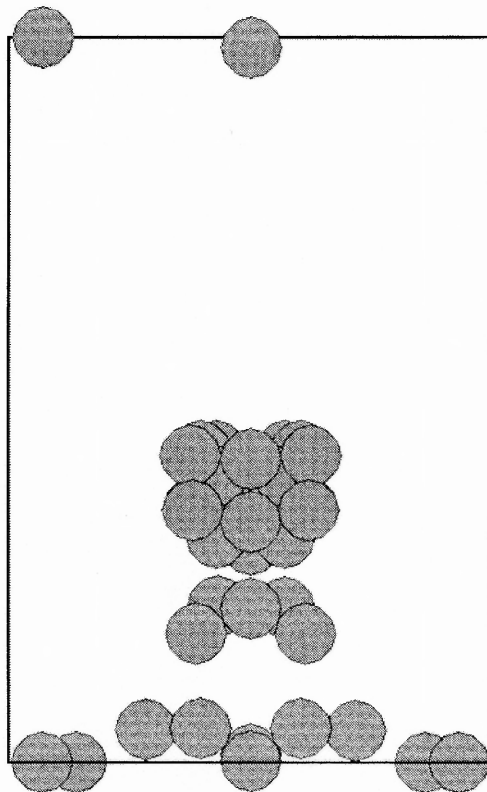


Figure 4.2.5.c The final position of the particles collected.

The above results imply that the regions in which the particles with $\beta < 0$ collect, i.e., the local minimums of $|\mathbf{E}|$, can be easily moved by changing the electrostatic potential of the electrodes. This, however, cannot be done when $\beta > 0$, since the particles always collect near the electrode edges for $\beta > 0$. The fact that the local minimums of $|\mathbf{E}|$ can be moved by changing the electric potential of the electrodes is important for applications which require that the particles be at a preset location for further manipulation. For example, in filtration related applications the particles must be collected in the regions from where they can be easily removed. Furthermore, by moving the position of the local minimum of $|\mathbf{E}|$, a set of particles can be moved along a predetermined trajectory in space. This is possible because the location of the minimum of $|\mathbf{E}|$ is determined by the electric potential boundary conditions which can be changed in a time dependent manner to have the local minimum at a given time, at a desired point. Moreover, since the particles near the local minimum can be moved along an arbitrary path by changing the electric potential boundary condition, an ER suspension, in principle, can be mixed by dragging the particles.

4.2.6 Variation With P_4

As discussed in chapter 2, the dimensionless parameter $P_4 = \frac{P_2}{P_3}$ determines the relative importance of the dipole-dipole interaction and dielectrophoretic forces. Specifically, when $P_4 = \frac{P_2}{P_3} = \frac{3\beta L}{16a}$ is large the dipole-dipole interactions dominate, which leads to the formation of particle chains. The formation of particle chains, as noticed before, is not desirable in filtration related applications because it slows down the motion of particles

and their eventual collection. On the other hand, when P_4 is small, the dielectrophoretic force dominates and the electrostatic particle-particle interactions are not sufficiently strong to form and hold the particle chains together. Consequently, the particles are easily separated from neighbors and move individually to the regions where the electric field is maximum or minimum. In order to isolate the role of the parameter P_4 , in this subsection, it will be assumed that the applied pressure gradient is zero.

From the definition of parameter P_4 , it is clear that it can be varied by changing the particle radius, the domain length and/or β . Also notice that β lies between -0.5 and 1.0, as it depends on the dielectric constants of the particles and the fluid, and that when β changes, P_2 and P_3 also change. In this section, P_4 will be varied using two different approaches: first by changing β and second by changing P_2 and P_3 . Notice that even though P_2 and P_3 cannot be varied independently for real ER fluids, the approach is useful for analyzing the mathematical nature of equations.

The two cases that assume $\beta = 0.01$ and 0.48 are discussed in this section. The dielectrophoretic forces are expected to dominate in the first case and the particle-particle interactions will be predominant in the second case. In the first case, the dielectric constants of the particles and the fluid are 7.3 and 7.5234694, respectively. The domain and particle sizes are the same as before. Two pairs of electrodes are used and the left electrodes are grounded whereas the right ones are at a potential of 1 V. Eighty particles are arranged in the domain in a periodic manner as shown in Figure. 4.1.a. The solids fraction is 0.118. The parameters Re , P_1 , P_2 , P_3 , Ma , P_4 and P_5 are 13, 0.342, 0.01, 0.342, 33.3, 0.03 and 1.0, respectively. Notice that if β is reduced, and all other parameters are

held fixed, both P_2 and P_3 decrease. In order to ensure that P_3 is the same as in section 4.2.2, the electric field strength is increased.

Our simulation show that all particles are collected near the electrode edges at $t = \sim 4.0$ s which is much smaller compared to the case described in section 4.2.2 where $P_4 = 0.89$. The time required in the present case is smaller because the particles, in this case, experience no chaining and move individually toward the electrode edges (Figure. 4.2.6.a).

For $\beta = 0.48$, the dielectric constants of the particles and the fluid are 7.3 and 270.1, respectively. As before, the magnitude of the dielectrophoretic force was kept fixed by adjusting the electric field strength. The initial arrangement of the particles is periodic and in the same manner as in the previous case. The parameters Re , P_1 , P_2 , P_3 , Ma , P_4 and P_5 are 463.1, 0.0096, 0.014, 0.0096, 0.69, 1.44 and 1.0, respectively. Simulations show that the particle chains are formed relatively quickly at $t = 0.3$ s and that these chains then move toward the electrode edges with a much smaller speed than for $\beta = 0.01$ (see Figure. 4.2.6.b). Also, notice that the chains, in this case, extend from one end of the domain to the other, which clearly shows that the electrostatic particle-particle interactions dominate.

Next, the case where the parameters Re , P_1 , P_2 , P_3 , Ma , P_4 and P_5 are 40.3, 0.111, 9.93×10^{-3} , 0.223, 11.2, 0.0446 and 2.0, respectively is considered. The magnitude of the parameter P_3 is increased by a factor of 2 and P_2 is decreased by a factor of 10, compared to their corresponding magnitudes in section 4.2.2. Since P_4 is much smaller than before, a much diminished tendency for the particles to form chains, is expected. The simulations

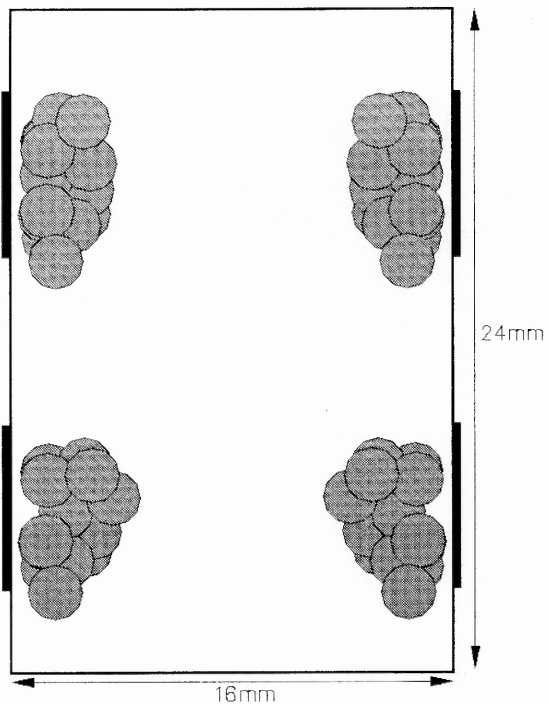


Figure 4.2.6.a The top view of the particle distribution at $t = 4.0$ s for the case where $P_4 = 0.03$.

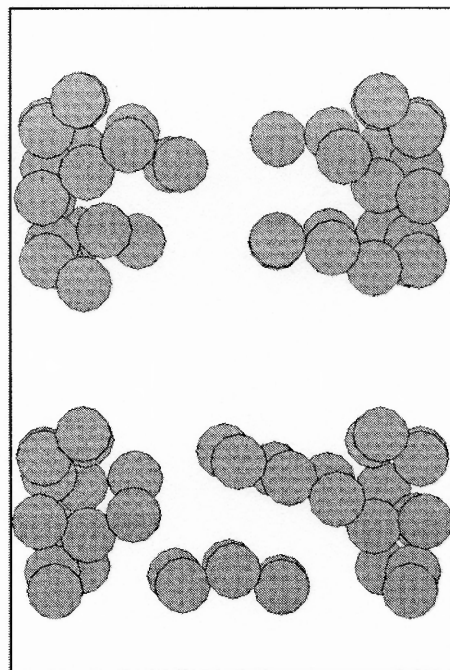


Fig. 4.2.6.b The top view of the particle distribution at time $t = 1.25$ s for the case where $P_4 = 2.7$.

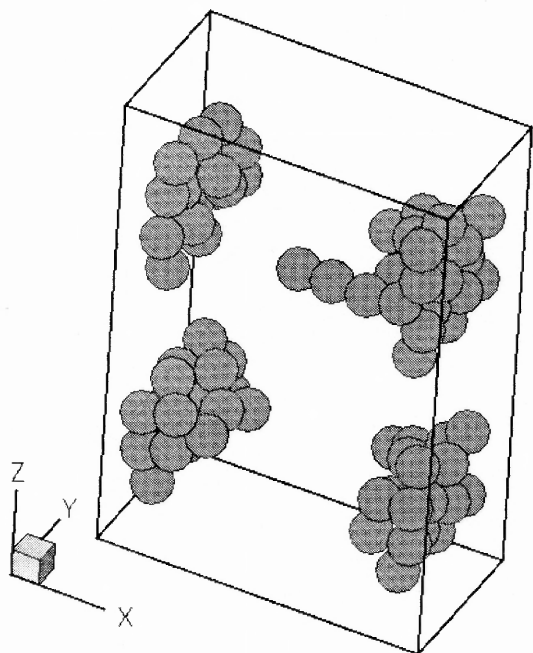


Fig. 4.2.6.c An oblique view of particles collected near the electrodes edges at $t = 5.29$ s.

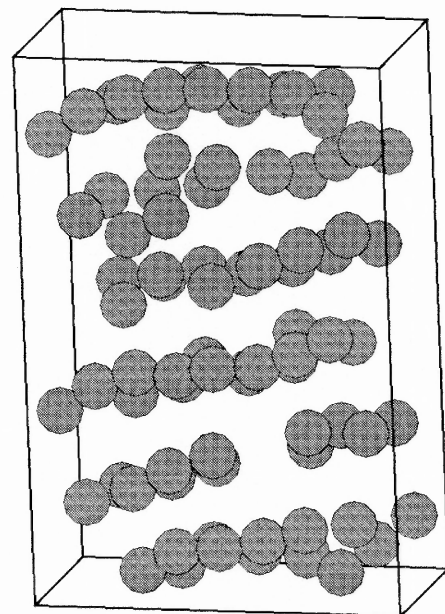


Fig. 4.2.6.d An oblique view of particle chains at $t = 3.08$ s

are performed by placing 80 particles in a domain with dimensions 1.6 mm x 0.8 mm x 2.4 mm. There are four layers of particles in the y-direction.

After the simulations are started, the particles move relatively quickly toward the edges of the electrodes without forming chains, as can be seen in Figure. 4.2.6.c, and get collected there. All particles are captured by the electrodes at $t = \sim 5.29$ s. The final position of the particles is shown in Figure. 4.2.6.c.

Next, the case where the parameters Re , P_1 , P_2 , P_3 , Ma , P_4 and P_5 are 40.3, 0.111, 0.993, 0.0111, 0.112, 89.2 and 0.1, respectively, is considered. The parameter P_2 is 10 times larger while P_3 is 10 times smaller than their corresponding values in section 4.2.2, and hence P_4 is 100 times larger. Thus, the electrostatic particle-particle interactions are expected to dominate. The other parameters are the same as for the case described above.

Once the simulations are started, in contrast to the previous case, the particles form chains, instead of individually moving to the electrodes. This can be observed from Figure. 4.2.6.d, which shows the positions of the particles at $t = 3.08$ s. The chains of particles rearrange and some chains even merge to form longer chains. Notice that some chains extend from one electrode to the other, and after they are formed remain almost stationary.

CHAPTER 5

CONCLUSIONS

This is the first direct simulation study of electrorheological suspensions subjected to spatially non-uniform electric fields. In this numerical scheme the fluid and particle equations of motion are combined into a single combined weak equation of motion, eliminating the hydrodynamic forces and torques, which helps ensure the stability of the time integration scheme. The distributed Lagrange multiplier method (DLM) [18, 49] is used to constrain the flow inside particle boundaries to be rigid body motion while the electrostatic forces acting on the polarized particles are obtained using the point-dipole approximation [38]. The numerical scheme is verified by performing a convergence study which shows that the results are independent of both the mesh and time step sizes. The dimensionless equations are derived to show that the dynamical behavior of ER suspensions subjected to non-uniform electric fields depends on the solids fraction, the ratio of the domain size and particle radius, and four additional dimensionless parameters which respectively determine the relative importance of inertia, viscous, electrostatic particle-particle interaction and dielectrophoretic forces. The simulation results are used to arrive at the following conclusions:

1. The particles with $\beta > 0$ collect in the regions where the magnitude of the electric field is locally maximum, whereas the particles with $\beta < 0$ collect in the regions where the magnitude of the electric field is locally minimum. The dielectrophoretic effect thus can be used to separate mixtures containing two sets of particles for which the sign of β is different.

2. When the fluid and particle inertia is negligible, the parameter P_5 , defined to be the ratio of the dielectrophoretic and viscous forces, determines the time duration in which the particles are collected near the local maximums or local minimums of the electric field magnitude.
3. The parameter P_4 , defined to be the ratio of the electrostatic particle-particle interaction and dielectrophoretic forces, determines the tendency of the particles to form chains. The time taken to collect increases with increasing P_4 because when $P_4 > O(1)$ the formation of particle chains delays the process of collection. In contrast, when $P_4 < O(1)$, the particles move individually without forming chains and, thus, the time taken for collection is relatively smaller. The rate of collection also depends on the electric field boundary conditions.
4. The electric potential boundary conditions can be modified to change the regions of low electric field strength, and thus the locations where the particles with $\beta < 0$ collect. By changing the boundary conditions in a time dependent manner, the regions in which the particles with $\beta < 0$ collect can be moved as a function of time. The electric field maximum, on the other hand, is at the electrode corners.
5. For relatively small applied pressure gradients, the bulk flow assists in the collection of particles by pushing them out of the regions where the dielectrophoretic force is small. However, when the applied pressure gradient is too large, the flow prevents particles from collecting (in both the high and low electric field regions).

REFERENCES

- [1] Adriani, P. M., Gast, A. P., "A microscopic model of electrorheology," *Physics of Fluids* **31**, pp. 2757-2768, 1988.
- [2] Anderson, R. A., "Electrostatic forces in an ideal spherical-particle Electrorheological Fluid", *Langmuir* **10**, pp. 2917-2928, 1994.
- [3] Andrade, E. N., Dodd, C., *Nature* **143**, 26 (1939).
- [4] Atten, P., Boissy, C., Foulc, J.-N., 1997, "The role of conduction in Electrorheological fluids: from interaction between particles to structuration of suspensions," *Journal of Electrostatics*, 40&41, pp. 3-12, 1997.
- [5] Becker, F. F., Wang, X.-B., Huang, Y., Pethig, R., Vykoukal, J., Gascoyne, P. R. C., "The removal of human leukemia cells from blood using interdigitated microelectrodes," *Journal of Physics D: Applied Physics*, **27**, pp. 2659-2662, 1994.
- [6] Becker, F. F., Wang, X.-B., Huang, Y., Pethig, R., Vykoukal, J., Gascoyne, P. R. C., "Separation of human breast cancer cells from blood by differential dielectric affinity," *Proceedings of the National Academy of Sciences, USA*, **92**, pp. 860-864, 1995.
- [7] Brady, J. F., Bossis, G., "Stokesian dynamics," *Annual Review of Fluid Mechanics* **20**, pp. 111-157, 1998.
- [8] Bonnecaze, R. T. and Brady, J. F., "Yield stresses in electrorheological fluids," *Journal of Rheology* **36**, pp. 73-115, 1992.
- [9] Bonnecaze, R. T. and Brady, J. F., "Direct simulation of electrorheological suspension," *Journal of Chemical Physics* **96**, pp. 2183-2204, 1992.
- [10] Brady, J. F., Phillips, R. J., Lester, J. C., Bossis, G., "Dynamic simulation of hydrodynamically interacting suspension," *Journal of Fluid Mechanics* **195**, pp. 257-280, 1988.
- [11] Chrzan, M. J., Coulter, J. P., *International Journal of Modern Physics B* **6**, 2651 (1992).
- [12] Davis, L. C., "Finite-element analysis of particle-particle forces in lelectrorheological fluids," *Applied Physics Letters* **60**, pp. 319-321, 1992.
- [13] Davis, L. C., "Polarization forces and conductivity effects in electrorheological fluids," *Journal of Applied Physics* **72**, pp. 1334-1340, 1992.

- [14] Davis, L. C., "The metal-particle/insulating oil system: An ideal electrorheological fluid," *Journal of Applied Physics* **73**, pp. 680-683, 1993.
- [15] Duff, A. W., *Physics Review* **4**, 23 (1896).
- [16] Foulc, J-N., Atten, P., Felici, N., "Macroscopic model of interaction between particles in an electrorheological fluid," *Journal of Electrodynamics* **33**, pp. 103-112, 1994.
- [17] Gast, A. P., Zukoski, C. F., "Electrorheological fluids as colloidal suspensions," *Advances in Colloid Interface Science* **30**, pp. 153-202, 1990.
- [18] Glowinski, R. T., Pan, W., Hesla, T.I and Joseph, D.D., "A distributed Lagrange multiplier/fictitious domain method for particulate flows," *International Journal of Multiphase Flows*. **25**, pp. 755-794, 1998.
- [19] Gong, H. and Lim, M. K., *Journal of Intelligent Material System and Structures* **7**, 89 (1996).
- [20] Green, N. G., Morgan, H., "Dielectrophoresis of submicrometer latex spheres. 1. Experimental results," *Journal of Physical Chemistry B*, **103**, pp. 41-50, 1999.
- [21] Green, N. G., Ramos, A., Morgan, H., "AC electrokinetics: a survey of sub-micrometer particle dynamics," *Journal of Physics D: Applied Physics* **33**, pp. 632-641 2000.
- [22] Green, N. G., Ramos, A., Morgan, H., "Numerical solution of dielectrophoretic and traveling wave forces for interdigitated electrode arrays using the finite element method," *Journal of Electrodynamics*, **56**, pp. 235-254, 2002.
- [23] Gulley, G. L., Tao, R., "Static shear stress of electrorheological fluids," *Physical Review E*, **48**, pp. 2744-2751, 1993.
- [24] Hao, T., "Electrorheological suspensions," *Advances in Colloid and Interface Science* **97**, pp. 1-35, 2002.
- [25] Hao, T., "Dynamic-field-induced oscillatory dc current in colloidal crystallite," *Journal of Physical Chemistry* **102**, pp. 1-3, 1998.
- [26] Hao, T., Kawai, A., Ikazaki, F., "The yield stress equation for electrorheological fluids," *Langmuir* **16**, pp. 3058-3066, 2000.
- [27] Hao, T., Kawai, A., Ikazaki, F., "Mechanism of electrorheological effect: evidence from the conductive, dielectric and surface characteristics of water-free electrorheological fluids," *Langmuir* **14**, pp. 1256-1262, 1998.

- [28] Hao, T., Xu, Y., "Conductive behavior of polymer-based electrorheological fluids under zero and oscillatory mechanical fields," *Journal of Colloid Interface Science* **181**, pp. 581-588, 1996.
- [29] Hughes, M. P., Morgan H., "measurement of bacterial flagellar thrust by negative Dielectrophoresis," *Biotechnology Progress*, **15**, pp. 245-249, 1999.
- [30] Hughes, M. P., Morgan H., Rixon, J. F., "Measuring the dielectric properties of herpes simplex virus type 1 virions with dielectrophoresis," *Biochimica et Biophysica Acta*, **1571**, pp. 1-8, 2002.
- [31] Jones, T. B., "Electromechanics of particles," *Cambridge University Press*, 1995.
- [32] Khusid, B., Acrivos, A., "Effects of conductivity in electric-field-induced aggregation in electrorheological fluids," *Physics Review E* **52**, pp. 1669-1693, 1995.
- [33] Klass, D. L., Martinek, T. W., "Electroviscous fluids II. Electrical properties," *Journal of Applied Physics* **38**, pp. 75-80, 1967.
- [34] Klingenberg, D. J., "Simulation of the dynamic oscillatory response of electrorheological suspensions: Demonstration of relaxation mechanism," *Journal of Rheology* **37**, pp. 199-214, 1993.
- [35] Klingenberg, D. J., van Swol, S., Zukoski, C. F., "The small shear rate response of electrorheological suspensions. I. Simulations in the point-dipole limit," *Journal of Chemical Physics* **94**, pp. 6160-6167, 1991.
- [36] Klingenberg, D. J., van Swol, S., Zukoski, C. F., "The small shear rate response of electrorheological suspensions. II. Extension beyond the point-dipole limit," *Journal of Chemical Physics* **94**, pp. 6170-6178, 1991.
- [37] Klingenberg, D. J., Zukoski, C. F., "Studies on the steady-shear behaviour of electrorheological suspensions," *Langmuir*. **6**, pp. 15-24, 1990.
- [38] Klingenberg, D. J., Zukoski, C. F., Hill, J. C., "Kinetics of structure formation in electrorheological suspensions," *Journal of Applied Physics* **73**, 4644-4648, 1993.
- [39] Lukkarnen, A. and Kaski, K., "Simulation studies of electrorheological fluids under shear, compression, and elongation loading," *Journal of Applied Physics* **83**, pp. 1717, 1998.
- [40] Markx, G. H., Dyda, P. A., Pethig, R., "Dielectrophoretic separation of bacteria using a conductivity gradient," *Journal of Bio Technology*, **51**, pp. 175-180, 1996.

- [41] Marshall, L., Goodwin, J.W., Zukoski, C. F., "Effects of electric fields on the rheology of non-aqueous concentrated suspensions," *Journal of Chemical Society Faraday I* **85**, pp. 2785-2795, 1989.
- [42] Melrose, J. R., *Molecular Physics*, **76**, 635 (1992).
- [43] Morgan, H., Hughes, M. P., Green, N. G., "Separation of submicron bioparticles by dielectrophoresis," *Biophysics Journal*, **77**, pp. 516-525, 1999.
- [44] Parthasarathy, M., Klingenberg, D. J., "Electrorheology: mechanisms and models," *Materials Science and Engineering R* **17**, pp. 57-103, 1996.
- [45] Pohl, H. A., Dielectrophoresis, Cambridge University press, Cambridge, UK, 1978.
- [46] See, H., Doi, M., "Shear-resistance of electrorheological fluids under time-varying electric fields," *Journal of Rheology* **36**, pp. 1143-1163, 1992.
- [47] See, H., Tamura, H., Doi, M., "The role of water capillaries in electrorheological fluids," *Journal of Physics D: Applied Physics* **26**, pp. 746-752, 1993.
- [48] See, H., Tamura, H., Doi, M., "Model of porous particles containing water in electrorheological fluids," *Journal of Physics D: Applied Physics* **26**, pp. 1181-1187, 1993.
- [49] Singh, P., Joseph, D. D., Hesla, T. L., Glowinski, R. T. and Pan, W., "A distributed Lagrange multiplier/fictitious domain method for particulate flows," *Journal of Non-Newtonian Fluid Mech* **91**, pp. 165-188, 2000.
- [50] Siu, Y. L., Jones, T. K., Wan, Yu, K.W., "Interparticle force in polydisperse electrorheological fluids: Beyond the dipole approximation," *Computer Physics Communications* **142**, pp. 446-452, 2001.
- [51] Stangroom, J. E., "Basic considerations in flowing electrorheological fluids," *Journal of Statistical Physics* **64**, pp. 1059-1072, 1991.
- [52] Stangroom, J. E., "Basic observations on electrorheological fluids," *Journal of Intelligent Material Systems and Structures* **7**, pp. 479-483, 1996.
- [53] Tang, X., Wu, C., Conrad, H., "On the conductivity model for the electrorheological fluid," *Journal of Rheology* **39**, pp. 1059-1073, 1995.
- [54] Tao, R., "electric-field-induced phase transition in electrorheological fluids," *Physical Review E*, **47**, pp. 423-426, 1993.
- [55] Tao, R., Sun, J. M., "Three-dimensional structure of induced electrorheological

- solid”, *Physics Review Letters* **67**, pp. 398-401, 1991.
- [56] Tao, R., Qi Jiang, “Simulation of structure formation in an electrorheological fluid,” *Physics Review Letters* **73**, pp. 205-208, 1994.
- [57] Uejima, H., “Dielectric mechanism and rheological properties of electrofluids,” *Japanese Journal of Applied Physics* **11**, pp. 319-326, 1972.
- [58] Washizu, M., Kurosawa, O., Arai, I., Suzuki, S., “Applications of electrostatic stretch-and-positioning of DNA,” *IEEE Transactions on Industrial Applications*, **30**, pp. 835-843, 1995.
- [59] Wen, W., Zheng, D. W. and Tu, K. N., “Chain/column evolution and the corresponding electrorheological effect,” *Journal of Applied Physics* **85**, pp. 530, 1999.
- [60] Winslow, M. W., “Induced fibrillation of suspensions,” *Journal of Applied Physics* **20**, pp. 1137-1140, 1949.
- [61] Wu, C. W., Conrad, H., “A modified conduction model for the electrorheological effect,” *Journal of Physics D: Applied Physics* **29**, pp. 3147-3153, 1996.
- [62] Wu, C. W., Conrad, H., *Material Science and Engineering* **A255**, 66 (1998).
- [63] Zukoski, C. F., “Material properties and the electrorheological response,” *Annual Review of Material Science* **23**, pp. 45-78, 1993.